

# Registration of Images With Varying Topology Using Embedded Maps

Xiaoxing Li\*, Xiaojing Long, Paul Laurienti, Christopher Wyatt, and  
ALZHEIMER'S DISEASE NEUROIMAGING INITIATIVE

**Abstract**—This paper presents registration via embedded maps (REM), a deformable registration algorithm for images with varying topology. The algorithm represents 3-D images as 4-D manifolds in a Riemannian space (referred to as embedded maps). Registration is performed as a surface evolution matching one embedded map to another using a diffusion process. The approach differs from those existing in that it takes an *a priori* estimation of image regions where topological changes are present, for example lesions, and generates a dense vector field representing both the shape and intensity changes necessary to match the images. The algorithm outputs both a diffeomorphic deformation field and an intensity displacement which corrects the intensity difference caused by topological changes. Multiple sets of experiments are conducted on magnetic resonance imaging (MRI) with lesions from OASIS and ADNI datasets. These images are registered to either a brain template or images of healthy individuals. An exemplar case registering a template to an MRI with tumor is also given. The resulting deformation fields were compared with those obtained using diffeomorphic demons, where topological changes are not modeled. These sets of experiments demonstrate the efficacy of our proposed REM method for registration of brain MRI with severe topological differences.

**Index Terms**—Deformable registration, false deformation, Riemannian embedding, topological change.

## I. INTRODUCTION

**D**EFORMABLE registration with high-degree-of-freedom transformations is the foundation of computational anatomy (CA) [1]. In neuroimaging CA methods include the

Manuscript received July 20, 2011; revised September 25, 2011; accepted November 24, 2011. Date of publication December 20, 2011; date of current version March 02, 2012. This work was supported by the National Institutes of Health through the NIH Roadmap for Medical Research, Grant U54 RR021813. Portions of the data collection and sharing for this project were funded by the Alzheimer's Disease Neuroimaging Initiative (ADNI; Principal Investigator: Michael Weiner; NIH Grant U01 AG024904). ADNI is funded by the National Institute on Aging, the National Institute of Biomedical Imaging and Bioengineering (NIBIB), and through generous contributions from the following: Pfizer Inc., Wyeth Research, Bristol-Myers Squibb, Eli Lilly and Company, GlaxoSmithKline, Merck and Co. Inc., AstraZeneca AB, Novartis Pharmaceuticals Corporation, Alzheimer's Association, Eisai Global Clinical Development, Elan Corporation plc, Forest Laboratories, and the Institute for the Study of Aging, with participation from the U.S. Food and Drug Administration. Industry partnerships are coordinated through the Foundation for the National Institutes of Health. The grantee organization is the Northern California Institute for Research and Education, and the study is coordinated by the Alzheimer's Disease Cooperative Study at the University of California, San Diego. ADNI data are disseminated by the Laboratory of NeuroImaging at the University of California, Los Angeles

\*X. Li is with GE Global Research, Niskayuna, NY 12309 USA (e-mail: lixia@ge.com).

X. Long and C. Wyatt are with the Department of Electrical and Computer Engineering, Virginia Polytechnic Institute and State University, Blacksburg, VA 24061 USA (e-mail: longxj@vt.edu; clwyatt@vt.edu).

P. Laurienti is with the Department of Radiologic Sciences, Wake Forest University, Winston-Salem, NC 27157 USA (e-mail: plaurien@wfbmc.edu).

Color versions of one or more of the figures in this paper are available online at <http://ieeexplore.ieee.org>.

Digital Object Identifier 10.1109/TMI.2011.2178609

various forms of morphometry [2]–[4], and have been widely used to study structural differences among brains and brain regions due to genetics, environment, and disease (see [5] and the references therein).

Image models of intact brains (excluding surgical resection) typically assume that the brain is a collection of shapes with a fixed topology representing distinct tissue types, gray matter (GM) and white matter (WM), modulated by a bias field and corrupted by additive noise (e.g., [6], [7]). This model holds reasonably well in the cortex of healthy young (postadolescent) subjects with limited shape variation (a small deformation model).

However, in the case of older subjects, both with and without manifest disease symptoms, the tissue shape and composition is much more complex. In these subjects, the changes most often seen in the clinic are large variations in the size and shape of ventricles, most likely because of tissue loss in the adjoining WM, as well as more subtle variations in subcortical shape, and cortical thickness (a large deformation model) [8]. Accompanying this increase in shape variation are changes in tissue composition that manifest as both diffuse and focal intensity differences. These intensity changes need not be accompanied by symptoms. For example WM hypo- and hyper-intensities have long been noted in T1 and T2 weighted images of older subjects (Leukoaraiosis) [9].

Intensity changes between images that cannot be modeled as bias or noise adversely influence registration algorithms. Such *topological changes* can cause *false deformation* in the resulting dense vector fields of existing deformable registration algorithms [10]. Consequently, in subsequent analysis such as deformation based morphometry (DBM), false deformation will be wrongly associated with local growth or shrinkage [11]. Prior work using morphology largely neglects this complication. In some studies, subjects with gross structural abnormalities are excluded (e.g., [12]), which may or may not exclude abnormal appearing tissue but likely does exclude widespread Leukoaraiosis or focal lesions. However, in clinical populations such changes of tissue contrast are common. Thus, image-based assessment tools must be able to account for tissue with abnormal appearance. The necessity of isolating the impact of topological changes in deformable registration has been demonstrated in previous works [13], using Cost Function Masking (CFM) [14]. CFM has been applied to parametric registration methods, for example, on cosine transform bases. The extension of CFM to nonparametric methods is not straightforward due to the severely increased dimensionality of the optimization space. However, some ongoing work is exploring this approach [15].

Assuming that such regions can be identified ahead of time (lesion segmentation), then their influence can be reduced. This

can be accomplished by registering topology corrected images rather than the original images, either through semi-manual labeling of the lesions [16] or through detecting and removing topological changes automatically [10]. However, since segmentation and registration are intimately connected, any issue that confounds segmentation and registration is problematic. Diffuse intensity changes are such a confound since defining a criteria for what constitutes a lesion, as required by segmentation, is arbitrary. Furthermore in WM regions near the cortex, abnormal WM may be classified as cortical GM. This misclassification propagates to the topologically corrected segmented image, which can lead to artificially increased cortical thickness.

In some applications, precomputed pathology models obtained from a group of training data can be used to account for topological changes, for example, in tumors [17]. However, the requirement for having such training data limits their application. Further, the precomputed model is specific to certain pathology and must be adapted on a per-case basis. In addition, several other methods have been developed to register brain images after surgical resection by matching subvolumes [18], [19], landmarks [20], segmentation surfaces [21], and adapting the EM framework [22], [23]. However the EM-based methods are generally limited to lower degree-of-freedom transformations due to the computational complexity involved.

Another approach is to model each topological change as a diffusion source or sink. Cuzol *et al.* used this approach in 2D to register images of Multiple Sclerosis patients [24] by using vortex particles to represent divergence of the deformation field. In a similar vein, the work by Risholm *et al.* [25] used anisotropic diffusion instead of Gaussian smoothing in a Demons registration framework regulated by diffusion sinks to generate a deformation field that was free of resection effects. Since each lesion must be modeled as a source or sink this approach introduces a heavy computational burden. Alternatively, a shape deformation and an intensity correction can be computed using the active appearance models [26]. The challenge with such method is that it needs a comprehensive training set, which properly covers a large variety of topological changes, for the construction of an appearance model.

Previous work most closely related to that presented here is that of metamorphosis theory [27]. A metamorphosis is a Riemannian metric defined on the space of images that measures both geometric deformation and intensity changes. Computation of a geodesic for this metric in the space of images leads to a partial differential equation (PDE) whose solution provides a diffeomorphism optimal up to an image residual error. The magnitude of the residual error is controlled via a spatially homogeneous parameter. This approach has been used in medical image averaging [28] and recently for brain atlas estimation [29]. However, because the allowed residual is spatially homogeneous, metamorphosis is not designed to minimize false deformation.

In previous work we developed a registration algorithm via embedding images into higher dimensional Riemannian space [30], [31]. The algorithm was used to register 2-D images without specifically suppressing false deformation. In this paper we extend this approach, named registration via embedded maps (REM), to handle topological changes by

suppressing their impact on the deformable registration process for 3-D brain MRI. Specifically, images in  $\mathbb{R}^3$  Euclidian space are embedded as surfaces in an  $\mathbb{R}^4$  Riemannian space. The registration process is then conducted as surface deformation, where the first three dimensions of the resulting deformation field correspond to the spatial grid deformation in the  $\mathbb{R}^3$  Euclidean space, and the fourth dimension corresponds to the intensity displacement. The contribution includes two aspects. First, compared with metamorphosis, our embedding models the two types of deformation in a metamorphosis, i.e., a spatial deformation and a template evolution, with a single PDE evolution in a higher dimensional space. This guarantees a smooth convergence of the diffusion to a local minimum. Second and more importantly, by carefully choosing a feature-space in the embedding, we are able to control the distribution of the deformation energy in a way that topological changes are mainly attributed to intensity displacement, while brain structural changes are mostly captured by spatial grid deformation. In doing so, topological changes do not impact the spatial deformation and thus false deformation is effectively suppressed. The resulting spatial deformation is a diffeomorphism, evolved using the intrinsic update step, as proposed in [32]. Note that, using our proposed algorithm, the structural shape difference of the brain anatomy is fully captured by the spatial deformation field, free from the impact of topological changes. Therefore, the resulting spatial deformation field can be independently used in CA methods on brain shape analyses, such as DBM.

During the preparation of this manuscript we became aware of a very similar approach by Zosso *et al.* [33], named Geodesic Active Fields, where 2D images are also registered in a Riemannian space and the deformation field is solved through a minimal surface flow corresponding to the harmonic map. The focus of that work was on general 2D imaging applications, where the work described in this paper was focused on using a similar approach for handling topological changes in 3-D brain MRI. Thus, although developed independently, the papers are complementary.

The rest of this paper is organized as follows. Section II provides relevant background. In Section III, we describe each component of our registration method and then summarize it into a registration algorithm. Experiments and results are given in Section IV. Section V discusses the limitations of, and alternatives to, the registration approach and concludes the paper.

## II. BACKGROUND

In this section, we explain several key concepts adopted by our proposed method, as well as give a brief introduction to the nonlinear diffusion framework.

### A. Topological Change and False Deformation

Healthy brains include normal classes of WM, GM, and CSF. In contrast, aging- and disease-induced brain MRI intensity changes can be referred to as *topological changes*. The new intensity class associated with such topological changes, together with the normal brain structural difference, drive deformation during deformable registration. In the resulting deformation field, part of the deformation that is caused by the altered

intensity, rather than the brain structural shape difference, is referred to as *false deformation* [10]. This definition of false deformation is somewhat ad hoc since topological changes result from various types of pathologies and associated tissue alterations. For example, space occupying lesions, such as a tumor, are associated with local deformation of surrounding tissue. However, this is not the case for tissue characteristic changes, such as multiple sclerosis, which do not cause local deformation. Without knowing their nature, we simply refer to all topological change-induced deformation as false deformation, which can be alternatively considered as uncertain deformation or deformation with unknown causes.

False deformation cannot be directly handled by typical registration methods. The reason is two-fold. First, it is hard for a registration algorithm to handle topological changes without pre-determining their pathological nature. Hence, some local deformation around topological changes is always expected to occur as their efforts to minimize intensity profile difference between images. Second, it is well known that the correctness of a deformation between two clinical images is in general not accessible due to the lack of a ground truth. It is therefore similarly difficult to distinguish *false portion* from an otherwise true deformation field. If images are registered using typical methods without properly handling topological changes, false deformation can no longer be separated from the overall deformation field in the postprocessing.

Due to these reasons, we adopted a new methodology in this work, where lesion segmentation is taken as part of the input, such that registration is performed *as if* the lesion had not been present. This idea is illustrated in Fig. 1. Assume we are trying to register the shape in Fig. 1(a) and (b), and the pathology of the topological change (big black dot) presented in Fig. 1(b) is unknown. If the two images are directly registered using a typical registration method, we will end up with a deformation field similar to the one shown in Fig. 1(c). The deformation represented by blue arrows corresponds to the structural difference between the circle and the square, and thus represents relatively *true* deformation. However, deformation represented by red arrows attempt to shrink the black dot in Fig. 1(b) to match the intensity profile in Fig. 1(a). As we mentioned above, this is regarded as false deformation. If the black dot had been caused by tissue characteristic change, the deformation represented by red arrows should ideally not exist. If space occupying lesion had been the reason for the black dot, it is possible that the deformation energy is asymmetric in the case where one side of the lesion grows faster than the other. One universal way of handling these cases is to not allow topological change to cause any deformation, which in this example leads to a deformation field as shown in Fig. 1(d). This resulting deformation field is useful in clinical applications since it registers all nonlesion tissue. For instance, images of different dementia patients can be registered to the same template without being affected by the hyperintensity lesions, which enables the subsequent analysis of shape difference of cortex. Another example is that the structural shape of a series of images with progressing tumor can all be registered to an image at a healthy stage, after which the relative volume of tumor can be assessed. After this registration step, if necessary, a tumor progression model can be further applied to reveal

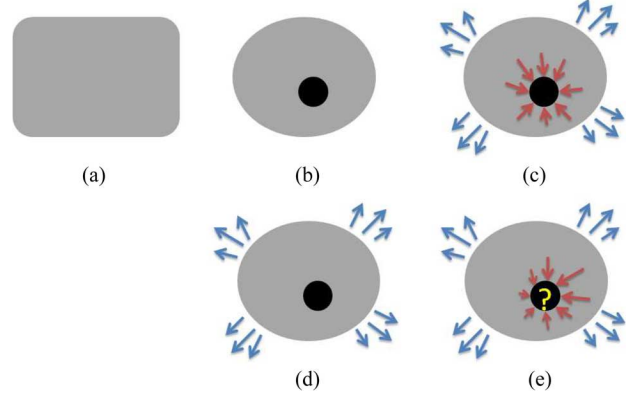


Fig. 1. Illustration of false deformation. (a) Image with normal topology. (b) Image with topological change. (c) Typical registration of (a) and (b) leads to false deformation (red arrows). (d) Registration result with suppression of the impact of topological change. (e) If tumor progression model being used suggests one side of the tumor grows faster than the other, the corresponding red arrows should differ in their lengths.

how its surrounding tissue deforms. This idea is demonstrated in Fig. 1(e), where we see that if the tumor progression model suggests that one side of the tumor grows faster than the other, the red arrows of the registration result should reveal this model and look like the ones shown in Fig. 1(e).

### B. Sochen–Kimmel–Malladi General Nonlinear Diffusion

Our algorithm is derived from the Sochen–Kimmel–Malladi general nonlinear diffusion [34], by choosing a particular embedding for our specific problem. The surface evolution follows the Euler-Lagrange equation that minimizes the surface weight measured by the Polyakov functional. Specifically, an image manifold  $(\Sigma, g)$  in  $\mathbb{R}^3$  is embedded as an  $\mathbb{R}^4$  feature-space manifold  $(M, h)$ , where  $g$  and  $h$  are the metric tensors on  $\Sigma$  and  $M$ , respectively. The map  $X : \Sigma \rightarrow M$  is chosen as

$$X = [x, y, z, I(x, y, z)] \quad (1)$$

where  $x, y, z$  are the local image Cartesian coordinates in  $\mathbb{R}^3$ , and  $I(x, y, z)$  is the intensity of the voxel at  $(x, y, z)$  in the image to be registered, referred to as the moving image,  $I_m$ , in the registration process. Based on a chosen map  $X$  and a metric  $h$ , the metric  $g$  is determined through the pullback procedure

$$g_{\mu\nu} = h_{ij} \partial_\mu X^i \partial_\nu X^j. \quad (2)$$

Note that (2) and subsequent equations use the Einstein notation (matching subscript and superscript variables are summed over), with  $\mu, \nu \in \{x, y, z\}$ ,  $i, j \in \{x, y, z, I\}$  for the given embedding. In (2),  $g_{\mu\nu}$  represents the  $(\mu, \nu)$  element of  $g$  and  $h_{ij}$  stands for the  $(i, j)$  element of  $h$ .

Using the above definitions, the surface area  $S$ , sometimes referred to as the weight of the map  $X$ , is calculated as

$$S[X^i, g_{\mu\nu}, h_{ij}] = \int d^m \sigma \sqrt{g} g^{\mu\nu} \partial_\mu X^i \partial_\nu X^j h_{ij} \quad (3)$$

where  $g^{\mu\nu}$  is the  $(\mu, \nu)$  element of  $g^{-1}$ ,  $\sqrt{g}$  is the square root of the determinant of the metric  $g$ , and  $m$  is the dimension of  $\Sigma$ .

This measure of the surface area is referred to as Polyakov functional in Riemannian geometry.<sup>1</sup> The variation of the Polyakov functional with respect to the embedding can be found by the Euler–Lagrange equation

$$-\frac{1}{2\sqrt{g}}h^{ij}\frac{\delta S}{\delta X^l} = \frac{1}{\sqrt{g}}\partial_\mu(\sqrt{g}g^{\mu\nu}\partial_\nu X^k) + \Gamma_{ij}^k\partial_\mu X^i\partial_\nu X^j g^{\mu\nu} \quad (4)$$

where  $\Gamma_{ij}^k, k, i, j \in \{x, y, z, I\}$  are the elements in the Levi–Civita connection, given by

$$\Gamma_{jk}^i = \frac{1}{2}h^{il}(\partial_j h_{lk} + \partial_k h_{jl} - \partial_l h_{jk}). \quad (5)$$

Note that the factor multiplied before  $\delta S/\delta X^l$  is to simplify the mathematical expression and does not change the minimization solution. Equation (4) defines the gradient descent direction that minimizes the Polyakov functional, which shrinks the embedded surface area most rapidly. Therefore, (4) is referred to as a minimal surface flow. It has been shown that many image processing tasks can be accomplished via minimizing the Polyakov functional, e.g., image smoothing and segmentation [34].

### III. REGISTRATION METHOD

In this work, we propose a registration algorithm via the minimization of the Polyakov functional. Our proposed algorithm differs from existing methods in the sense that it uses a segmentation of the topological changes as an input and is capable of registering brain MRI, while eliminating false deformation. The following describes the three major components of the proposed algorithm and then summarizes them into a registration algorithm.

#### A. Choice of Embedding

To establish a proper registration objective, we define the metric  $h$  in the following form:

$$h = \begin{bmatrix} \phi & 0 & 0 & 0 \\ 0 & \phi & 0 & 0 \\ 0 & 0 & \phi & 0 \\ 0 & 0 & 0 & \beta\phi \end{bmatrix} \quad (6)$$

where  $\phi$  is a positive function that influences the shape of a harmonic map by changing the physical meaning of the surface weight. While for a metric tensor, it is merely required to be positive-definite and symmetric, this diagonal matrix  $h$  holds the simplest mathematical form while maintaining the three coordinates of physical space uncorrelated. Additionally, using this diagonal form, the length measure on the surface will be simply scaled by function  $\phi$ . Thus, function  $\phi$  provides us with the flexibility of intuitively adjusting the path of diffusion, similar to geodesic surfaces [35], and enables the minimal surface flow to achieve the desired objective. The term  $\beta$  defines the feature-space of the embedding, which is the relative magnitude between image features and spatial domain.

Taking inspiration from geodesic active contours [36], we note that for a specific choice of metric, the Polyakov function measures the area of the surface in the space  $M$ . This gives us the freedom to use the fixed image of the registration to define

<sup>1</sup>We refer interested reader to [34] for detailed explanation on its physical meaning and its derivation.

the metric and thus influence the shape of the harmonic map. In this work, we choose  $\phi = (I_m - I_f)^2$ , where  $I_m$  and  $I_f$  are the moving and the fixed images, respectively. The squared image difference given by  $\phi$  is the most commonly used error measurement in intensity-based registration. The difference between our work and existing registration methods is that in our work,  $\phi$  is not directly minimized, rather it is used to modulate the metric  $h$ . Intuitively, consider an infinitesimal region on the embedded surface of the moving image, the value of  $\phi$  at this location scales the magnitude of the surface tensor, which in turn modulates the distance measure, and thus scales the surface area (surface weight) of this region. As a result, when using the error measure between the moving and the fixed images for the value of  $\phi$ , such as  $\phi = (I_m - I_f)^2$ , the embedded surface will have larger surface areas at locations where there are bigger differences between the two images. Consequently, when minimizing the surface area, the embedded surface of the moving image will shrink its area most rapidly at such locations. Eventually, the surface area, measured by the Polyakov functional, will achieve its minimum, where  $\phi$  has minimal-value everywhere, i.e., the moving and the fixed images are perfectly aligned. In other words, during the diffusion, the surface area is attracted by a potential well formed by  $\phi$ , and our particular choice of  $\phi$  transforms the Polyakov functional into a registration objective.

The factor  $\beta$  defines the relative magnitude between the feature and the geometric space. The choice of  $\beta$  impacts the distribution of deformation energy. This is illustrated in Fig. 2, where we use red and blue curves to represent surface cut profiles of a moving and a fixed image, respectively. The arrows denote the gradient directions evolving the moving surface to the fixed surface. In Fig. 2(a),  $\beta$  is set to a small value, and thus image intensity is weighted less in the pullback. When the moving image is evolved to the fixed image, the gradient direction will be better co-aligned with the intensity axis, and the deformation energy will be concentrated on intensity displacement. Alternatively as shown in Fig. 2(b), if  $\beta$  is set to a large value, the gradient direction of evolving the moving image to the fixed image will be better co-aligned with the spatial grid axis, and the deformation energy will be more distributed to the spatial deformation. Based on this intuition, if we have a function  $p(x, y, z)$ , whose value indicates the probability that the voxel at  $(x, y, z)$  lies within a region of topological change, we can construct the function  $\beta$  as

$$\beta(x, y, z) = \frac{1}{p(x, y, z) + \epsilon} \quad (7)$$

where  $\epsilon$  is a small positive value to avoid division-by-zero. With this function, for image regions with normal local topology,  $p(x, y, z)$  will have small values and  $\beta$  will have large values accordingly. We choose to use the inverse function instead of some other functions, for example  $1 - p(x, y, z)$ , since it leads to a sharper contrast between lesion and nonlesion regions, in terms of the values in  $\beta$ . Then the deformation in these regions will concentrate on the spatial grid to capture the structural difference between the moving and the fixed images. On the other hand, for image regions that do have topological change,

$p(x, y, z)$  will have large values and  $\beta$  small values, so that the intensity displacement is favored during the registration process to correct the tissue appearance.

### B. Computation of Surface Variation

In the following, we use a single subscript to denote first order derivative, e.g.,  $\phi_x$  is the partial derive of function  $\phi$  with respect to  $x$  coordinate. Note that  $\phi_I$  is the partial derivative of  $\phi$  with respect to the moving image. Double subscript means second-order partial derivative, e.g.,  $I_{xx}$  is the second order partial derivative of the moving image with respect to  $x$  coordinate. Using the map given in (1) and the metric in (6), we can obtain the metric  $g$  through the pullback procedure, (2)

$$g = \phi \begin{bmatrix} 1 + \beta I_x^2 & \beta I_x I_y & \beta I_x I_z \\ \beta I_x I_y & 1 + \beta I_y^2 & \beta I_y I_z \\ \beta I_x I_z & \beta I_y I_z & 1 + \beta I_z^2 \end{bmatrix}. \quad (8)$$

After the embedding, the registration is to be carried out by minimizing the conformal area given in (3). This leads to the following objective function:

$$\min_{\Omega=(s,\Delta)} S[X^i, g_{\mu\nu}(\Omega), h_{ij}(\Omega)] \quad (9)$$

where  $S[X^i, g_{\mu\nu}(\Omega), h_{ij}(\Omega)]$  is given by (3).  $h_{ij}$  and  $g_{\mu\nu}$  are given in (6) and (8), respectively. Further,

$$\phi = (\Omega I_m - I_f)^2 = [(I_m \circ s + \Delta) - I_f]^2 \quad (10)$$

with a spatial deformation  $s$  and an intensity displacement  $\Delta$ . Again, we emphasize that, the optimization over the search space  $\Omega$  is achieved *jointly* over  $(s, \Delta)$  in a single optimization framework. In other words, we are *not* solving the problem by separating  $s$  and  $\Delta$  and seeking for their individual optima in an iterative back-and-forth manner. This is a key point that differs our method from existing ones. Using the result from Sochen–Kimmel–Malladi diffusion in (4), the gradient direction of the above minimization is given by

$$\frac{\partial X}{\partial t} = \frac{\phi^2}{\sqrt{g}} \partial_\mu (\sqrt{g} g^{\mu\nu} \partial_\nu X^k) + \phi^2 \Gamma_{ij}^k \partial_\mu X^i \partial_\nu X^j g^{\mu\nu}. \quad (11)$$

Here,  $t$  is the time variable that represents a step in the diffusion process. Note that in (11), the Euler–Lagrange equation is multiplied by  $\phi^2$  to simplify the expression. Since it is a strictly positive function, the multiplication will not affect the solution. Collecting the above terms, we obtain the registration updating rule

$$\frac{\partial X}{\partial t} = S_1 \begin{bmatrix} -\beta I_x \\ -\beta I_y \\ -\beta I_z \\ 1 \end{bmatrix} + S_2 \begin{bmatrix} I_x \\ I_y \\ I_z \\ I_x^2 + I_y^2 + I_z^2 \end{bmatrix} + S_3 \begin{bmatrix} -\beta I_x \\ -\beta I_y \\ -\beta I_z \\ 1 \end{bmatrix} \quad (12)$$

where

$$\begin{aligned} S_1 &= \frac{\phi}{\kappa^2} [(1 + \beta I_y^2 + \beta I_z^2) I_{xx} + (1 + \beta I_x^2 + \beta I_z^2) I_{yy} \\ &\quad + (1 + \beta I_x^2 + \beta I_y^2) I_{zz}] \\ &\quad - \frac{2\phi\beta}{\kappa^2} (I_x I_y I_{xy} + I_x I_z I_{xz} + I_y I_z I_{yz}) \\ &\quad + \frac{3}{2\kappa} (\phi_x \beta I_x + \phi_y \beta I_y + \phi_z \beta I_z - \phi_I) \\ S_2 &= -\frac{\phi_I}{2\kappa} \\ S_3 &= -\frac{\phi}{2\kappa\beta} (\beta_x I_x + \beta_y I_y + \beta_z I_z) (1 + \kappa) \\ \kappa &= 1 + \beta I_x^2 + \beta I_y^2 + \beta I_z^2. \end{aligned}$$

Note that in (12), we intentionally assemble all the terms that are related to the partial derivatives of  $\beta$  in  $S_3$ . The first three dimensions in (12) define the spatial grid deformation that captures the structural differences between the moving and the fixed images. The fourth dimension in (12) defines the intensity displacement, which concentrates on the preidentified topological changes. The detailed derivation of (12) can be found in the Appendix. We want to emphasize that using (12), the distribution of the deformation energy in the intensity displacement and the spatial grid deformation can be directly controlled by the function  $\beta$ . This is the major reason that false deformation can be eliminated from the resulting deformation field. To better understand this, if we set  $\beta$  to extreme values of  $+\infty$  and 0, we can obtain the following two equations:

$$\lim_{\beta \rightarrow +\infty} \frac{\partial X}{\partial t} = [I_x H \quad I_y H \quad I_z H \quad 0]' \quad (13)$$

where the common term<sup>2</sup>

$$\begin{aligned} H &= -\frac{\phi I_x [(I_y^2 + I_z^2) I_{xx} + (I_x^2 + I_z^2) I_{yy} + (I_x^2 + I_y^2) I_{zz}]}{(I_x^2 + I_y^2 + I_z^2)^2} \\ &\quad - \frac{2\phi I_x (I_x I_y I_{xy} + I_x I_z I_{xz} + I_y I_z I_{yz})}{(I_x^2 + I_y^2 + I_z^2)^2} \\ &\quad - \frac{3I_x (\phi_x I_x + \phi_y I_y + \phi_z I_z)}{2(I_x^2 + I_y^2 + I_z^2)} \end{aligned}$$

and

$$\lim_{\beta \rightarrow 0} \frac{\partial X}{\partial t} = [I_x T \quad I_y T \quad I_z T \quad \infty]' \quad (14)$$

where the common term

$$T = \phi_I I_x - 2\phi I_x (\beta_x I_x + \beta_y I_y + \beta_z I_z).$$

It is easy to observe that (13) and (14) agree with our expectation (refer to Section III-A). In particular, when  $\beta$  has a very

<sup>2</sup>This case, i.e.,  $\beta \rightarrow +\infty$ , is known to be related to the mean curvature flow. Interested readers can refer to [34] for details

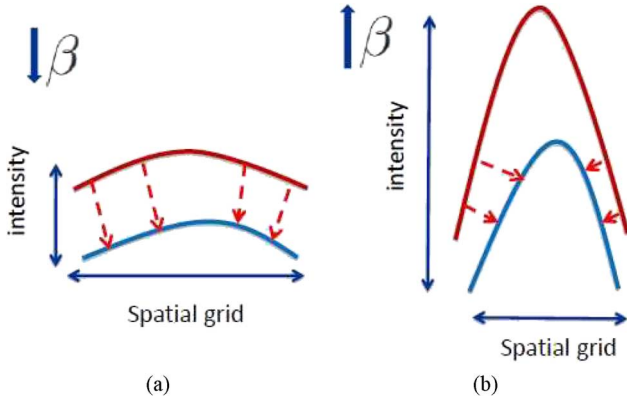


Fig. 2. Influence of  $\beta$  on the deformation field. Red and blue curves represent surface cut profiles of a moving and a fixed images, respectively. The arrows denote the gradient directions evolving the moving surface to the fixed surface. (a)  $\beta$  is set to a small value, and thus image intensity is weighted less in the pullback. When the moving image is evolved to the fixed image, the gradient direction will be better co-aligned with the intensity axis, and the deformation energy will be concentrated on intensity displacement. (b)  $\beta$  is set to a large value, the gradient direction of evolving the moving image to the fixed image will be better co-aligned with the spatial grid axis, and the deformation energy will be more distributed to the spatial deformation.

large value, the spatial grid deformation contains the most energy, whereas when  $\beta$  has a very small value, the intensity displacement dominates the deformation energy. Note that we do not require a precise lesion segmentation to form the  $\beta$  function. It can be based on any estimated probability function  $p(x, y, z)$ . In real applications,  $p(x, y, z)$  can be constructed from some lesion-likelihood measurements, or a smoothed version of a rough lesion segmentation, for example

$$p \doteq K_{\text{prob}} * L \quad (15)$$

where  $K_{\text{prob}}$  is a Gaussian kernel and  $L$  is the segmentation label map of topological changes. In most cases, after intensity displacement, the spatial deformation of the areas affected by topological changes will be filled by the interpolation of the deformation from their neighborhood, due to the smoothness constraints of the deformation field. Thus, when we construct  $\beta$  from a smoothed rough segmentation of the topological change, over- or under-segmentation have limited effects.

### C. Diffeomorphic Constraint

In medical image registration, regularization of the spatial transformation ensures a physically meaningful registration result. Most registration algorithms constrain the resulting deformation field to be in the group of diffeomorphisms [32], [37]. Diffeomorphisms are smooth invertible transformations with smooth inverse, which causes no tearing or folding of the physical space when being applied. Constraining the evolution of a deformation field to be within the group of diffeomorphisms also ensures a stable diffusion process by avoiding spikes when solving the associated PDE.

Ideally, in diffusion based methods, diffeomorphism can be obtained by physically constraining a positive Jacobian determinant, using a constrained optimization [37]. However, in our method, only the first three dimensions of the surface variation correspond to spatial deformation and are required to be diffeomorphism. The fourth dimension, on the other hand, is intensity

change and *should not* be confined in the group of diffeomorphism. This can be illustrated by a simple example. Imagine that, we have two pixels, the left and the right, on an input image. If the left pixel has a smaller intensity than that of the right one, diffeomorphism essentially ensures that after intensity displacement, the left pixel cannot change to a larger intensity than the right pixel, i.e., it maintains the “order” of the intensities of the two pixels. This is obviously not desirable in our algorithm. On the other hand, adding constraint only to some of the dimensions in a diffusion process is difficult, and to the best of our knowledge such a mathematical solution is not directly available. An alternative method, is to perform spatial deformation within a Lie group of diffeomorphism, as proposed in the work of diffeomorphic demons [32]. Then, the diffeomorphic registration can be performed under unconstrained optimization routines. Following this idea, we adopt the *intrinsic updating rule*

$$s \leftarrow s \circ \exp(u) \quad (16)$$

for the evolution of the spatial deformation field. Here,  $s$  is the vector field of the overall spatial deformation and  $u$  contains the first three components of the surface evolution in (12):  $u = [\partial X^1/\partial t \ \partial X^2/\partial t \ \partial X^3/\partial t]'$ . In the update rule,  $\exp(*)$  stands for the vector field exponential operation, which can be efficiently computed through iterative composition [32]. The intensity displacement, on the other hand, is directly accumulated as

$$\Delta \leftarrow \Delta + \delta \quad (17)$$

where  $\Delta$  is the overall intensity displacement, and  $\delta$  is the last component of the surface evolution in (12):  $\delta = \partial X^4/\partial t$ . The intensity displacement  $\Delta$  is applied to the fixed image  $I_f$  as

$$I_f^{t+\Delta t} = I_f + \Delta \quad (18)$$

where  $t$  is the time variable. Because the intensity difference caused by topological changes is reduced during this step, we refer to it as *intensity correction*.

### D. Registration Algorithm

To summarize, we have the following registration algorithm:

#### Algorithm: Registration via Embedded Maps (REM)

- Initialization:
  - 1) set image with normal topology as moving image  $I_m$ ;
  - 2) set image with topological changes as fixed image  $I_f$ ;
  - 3) construct  $\beta$  using a segmentation label map  $L$  using (15) and (7);
  - 4) set deformation field  $s = Id$  and intensity displacement  $\Delta = 0$ .
- Iteration  $t$ :
  - 1) Solve the optimization in (9) through surface evolution given in (12):
 
$$u = \left[ \frac{\partial X^1}{\partial t} \ \frac{\partial X^2}{\partial t} \ \frac{\partial X^3}{\partial t} \right]' \quad \text{and} \quad \delta = \frac{\partial X^4}{\partial t};$$
  - 2) apply fluid-like regularization on  $u$ :  $u \leftarrow K_{\text{fluid}} * u$ ;

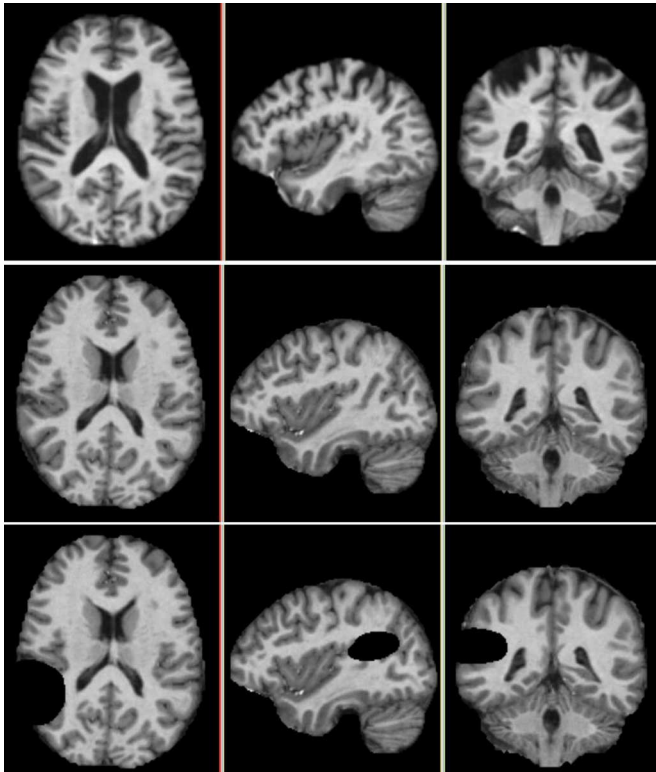


Fig. 3. Images used in this demonstrative experiments. First row, an elderly subject, referred to as *old*; second row, a young subject, referred to as *young*; third row, the young subject with a manually created resection, referred to as *resectioned*.

- 3) update deformation field:  $s \leftarrow s \circ \exp(u)$ ;
- 4) apply diffusion-like regularization on  $s$ :  $s \leftarrow K_{\text{diff}} * s$ ;
- 5) update intensity displacement:  $\Delta \leftarrow \Delta + K_{\text{int}} * \delta$ ;
- 6) apply spatial deformation:  $I_m^{t+1} = I_m \circ s$ ;
- 7) apply intensity displacement:  $I_f^{t+1} = I_f + \Delta$ ;
- 8) if (t == maxIteration) break;

In the algorithm,  $K_{\text{fluid}}$ ,  $K_{\text{diff}}$ , and  $K_{\text{int}}$  are all Gaussian smoothing kernels. The variances for  $K_{\text{fluid}}$ ,  $K_{\text{diff}}$  are selected in the same way as in Diffeomorphic Demons, where typical value is within [0.8, 1.2]. The variance of  $K_{\text{int}}$  has no direct impact on the convergence of the diffusion, and it only controls the spatial smoothness of the intensity displacement. We use a variance of 0.4 for  $K_{\text{int}}$  in all experiments. We choose to set a maximum number of iteration as the stopping criteria, following the convention in Diffeomorphic Demons. Note that under the intrinsic updating rule, the registration error typically begins to oscillate when the diffusion tends to become stable. This oscillation effect is a detectable pattern and can also be used as a stopping criteria.  $u$  and  $\delta$  are both normalized and multiplied by a chosen step size as typical in registration methods. The step size of  $u$  is related to the variance of  $K_{\text{fluid}}$  and  $K_{\text{diff}}$ , where larger step size can be used with larger smoothing kernels. Experimental setting of  $\delta$  is around 5% of estimated maximum intensity displacements.

#### IV. EXPERIMENTS AND RESULTS

In this section, the proposed registration algorithm REM was tested under multiple sets of experiments as commonly used

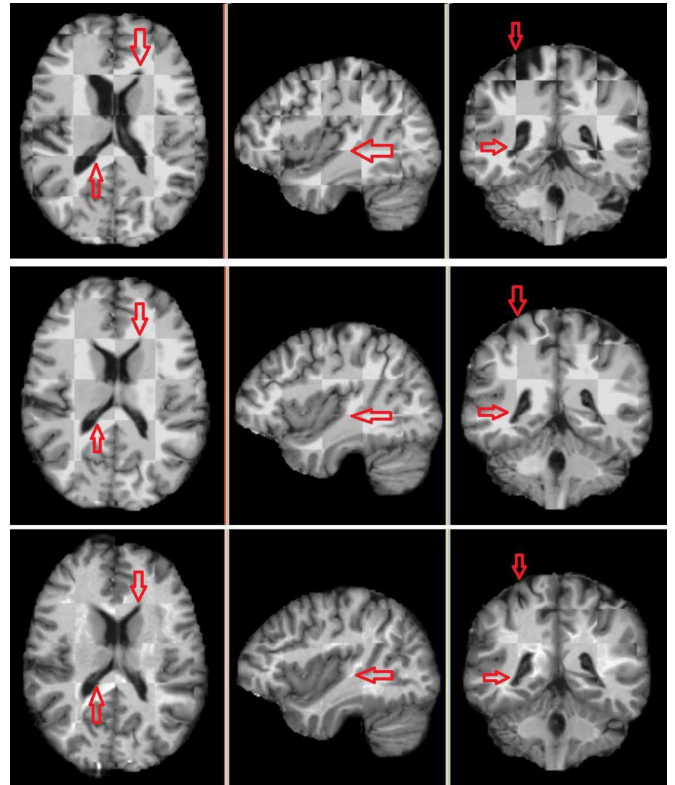


Fig. 4. Registration performance on images without topological change. The upper row shows the checkerboard image of old and young, before registration; the second row shows registration result using REM, which is the checkerboard image of the young and the deformed old, i.e., after applying spatial deformation to old; the third row shows the checkerboard image with registration result using diffeomorphic demons.

for structural brain MRI analysis. The resulting deformation fields were compared with those obtained using diffeomorphic demons [32], where topological changes are not modeled. Some additional results were provided to demonstrate the impact of false alarm and misdetection of topological changes in the construction of  $\beta$ . Experiments were also conducted for the cases where both moving and fixed images have topological changes to show limitations of the current algorithm.

##### A. Registering Images of With Synthetic Topological Change

In this subsection, we conduct a series of demonstrative experiments to highlight several key features of our registration algorithm. Specifically, we register the brain image of an elderly subject (referred to as *old*, shown in the first row in Fig. 3) to a pair of images of a young subject with and without a manually created resection (referred to as *young* and *resectioned*, shown in the second and third rows in Fig. 3, respectively), to get a direct and quantitative evaluation of the algorithm performance. Both young and old are T1 MRI from OASIS dataset, where young is taken for a healthy male at age 21, and old is from a healthy female at age 77.

First, we use our algorithm to register old and young. The purpose is to show that although our algorithm is motivated by the need for accurately registering images with topological changes, it can still be used to register images with normal topology,

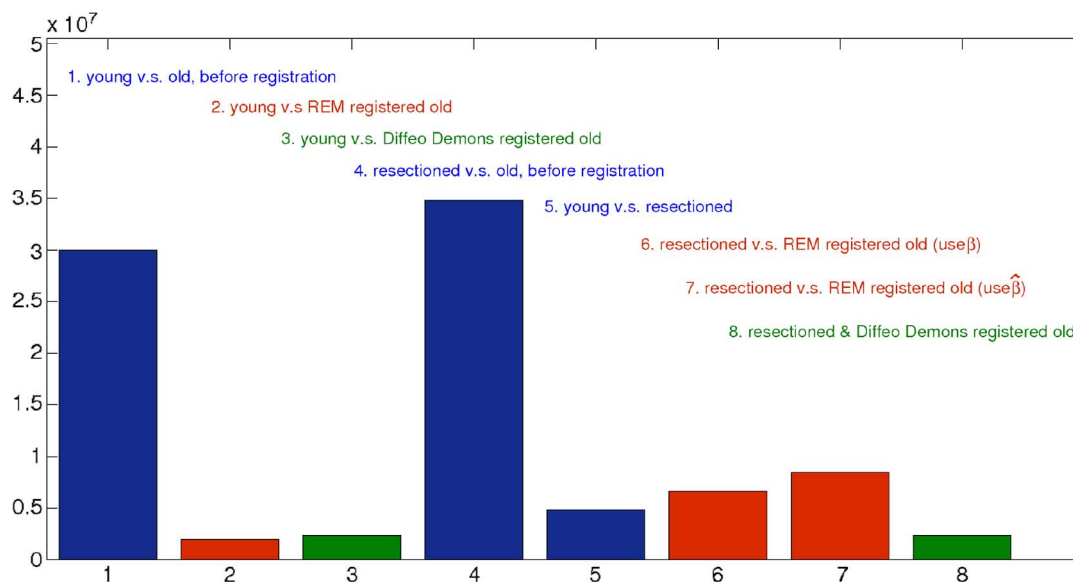


Fig. 5.  $L_2$  image residuals. Blues bars, residuals before registration. Red bars, residuals after REM registration. Green bars, residuals after diffeomorphic demons registration.

i.e., without topological changes. The spatial deformation, in this case, carries all the deformation energy, achieved by setting the lesion probability map  $p(x, y, z)$  to zero everywhere and not allowing intensity to deform. In the experiment, old is used as the moving image and young is used as the fixed. We used Gaussian kernels with  $\sigma_{\text{fluid}} = \sigma_{\text{diff}} = 0.8$  for  $K_{\text{fluid}}$  and  $K_{\text{diff}}$ .<sup>3</sup> For comparison purposes, we used diffeomorphic demons algorithm [32] to perform the same set of experiments. Three resolutions are used in the diffeomorphic demons, and 10, 20, and 100 iterations were performed in each resolution, respectively. The variances used in the Gaussian smoothing kernel for fluid and diffusion regularization are both set to 0.8, the same as in our algorithm. With this experiment setting, the computational load of the two algorithms is comparable. Fig. 4 shows the registration results of both methods. The upper row shows the checkerboard image of old and young, before registration. The middle row gives the registration result using our proposed REM, which is the checkerboard image of young and the deformed old, i.e., after applying spatial deformation to old. The lower row shows the checkerboard image of the registration result obtained by diffeomorphic demons. The three columns give the axial, sagittal and coronal views of the images, respectively. Note that, due to the large age difference, the two subjects used in this experiment have significant structural difference, which can be seen at the locations pointed out by the red arrows. From Fig. 4, it can be observed that both algorithms well aligned the two images after registration. The  $L_2$  image residuals of the original images and those registered ones using the two algorithms are shown as the first three bars in Fig. 5. We can see that there is a large  $L_2$  image residual between young and old before registration (bar 1), and this is minimized to approximately the same amount when the two registration algorithms are applied (bars 2 and 3, respectively).

<sup>3</sup>All the parameter settings are in voxel units. All the images from OASIS dataset have a spatial resolution of  $1 \text{ mm} \times 1 \text{ mm} \times 1.25 \text{ mm}$ . Those from ADNI dataset used in this work have a spatial resolution of  $1.2 \text{ mm} \times 1.2 \text{ mm} \times 1.25 \text{ mm}$ .

The glyph views of the deformation fields obtained via REM (the left) and diffeomorphic demons (the right) are shown in Fig. 6.<sup>4</sup> We find that although the two algorithms converged to comparable  $L_2$  image residuals, the shapes of the two deformation fields are different, due mainly to their respective optimization objectives. For REM, the spatial deformation energy mainly concentrates around the ventricle and several areas in the temporal lobe and occipital lobe. For diffeomorphic demons, however, the deformation energy is much more dispersed.

Second, we register old to resectioned. The image with resection is created by manually removing a large region of cortex from the healthy brain of young used above. The manually created image is then used as a probe, similar as the approach taken in [38], to conduct the same registration experiments. The same parameters as before are used, except that  $\beta$  was constructed with  $\sigma_{\text{prob}} = 1$  for  $K_{\text{prob}}$  in (15) and  $\epsilon = 0.01$  in (7). The manual mask used to create the resection is taken to form  $\beta$  function. The checkerboard images of the original images and after-registration ones using the above-mentioned parameters are given in the first two rows of Fig. 7. Using the registration results given in Fig. 4 as a reference, we see that for all the non-resection parts of the brain, our algorithm converges to an accurate alignment, i.e., visually almost identical to that obtained in Fig. 4 and unaffected by the big resection area.

In addition, we include another experiment to demonstrate how  $\beta$  function is used to selectively deform intensity only in regions with topological changes. Specifically, we substitute the  $\beta$  function with a uniform positive value  $\hat{\beta} = 0.5$ , and perform the registration with all other parameters being the same. The third row of Fig. 7 gives the checkerboard image of using this parameter setting. In this case, spatial and intensity deformation will evolve simultaneously over the entire image. Conceptually, under this setting, our algorithm will behave similarly as

<sup>4</sup>Note that the arrows in the glyph plot are only for illustrative purposes, and may not be in real voxel scale. In many cases, we increase their lengths for a clear visualization. This applies to all the following glyph plots throughout this work, unless mentioned otherwise.

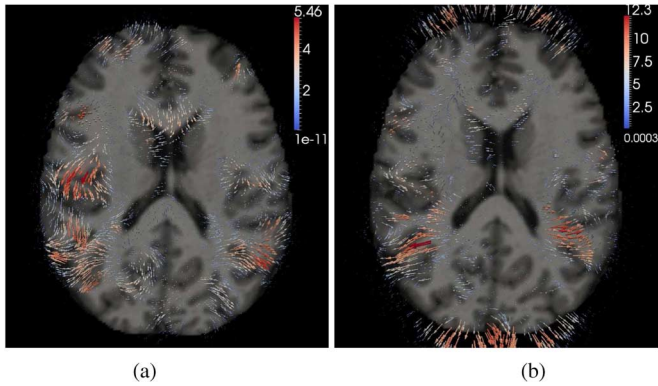


Fig. 6. Glyph views of the deformation fields obtained via REM (left) and diffeomorphic demons (right).

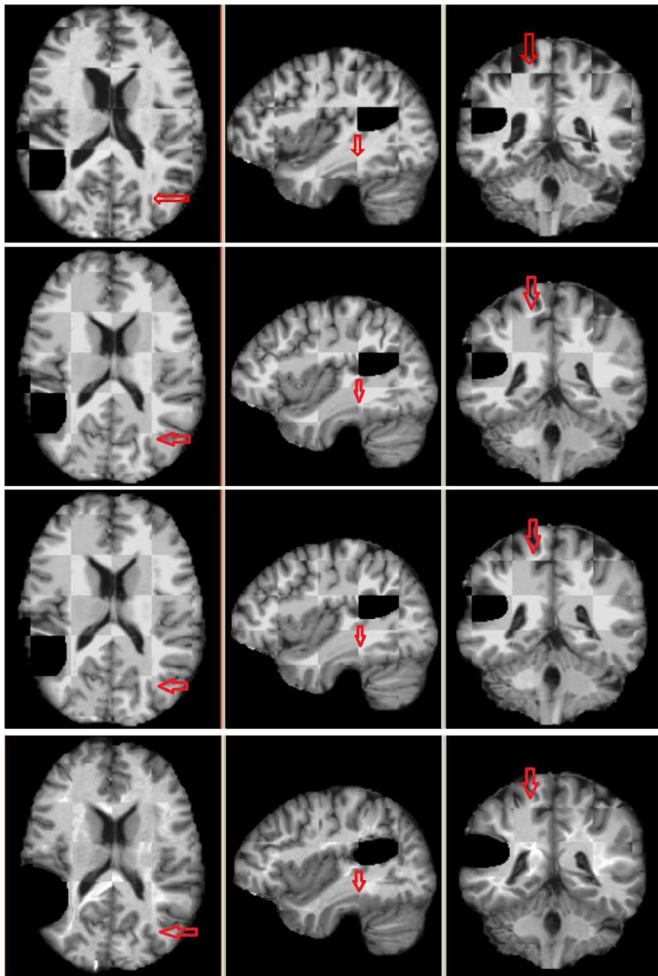


Fig. 7. Checkerboard image of registration results from old to resectioned. First row, before registration; second row, after REM registration, when resection mask is used to construct  $\beta$ ; third row, after REM registration, when uniform value  $\beta = 0.5$  is used; fourth row, after diffeomorphic demons registration.

the metamorphosis approach, or more generally speaking, similarly as all other methods with a spatial deformation evolution specified by  $u = |I_f - I_m| \cdot \nabla I_f$  and an intensity update given as  $\delta = (I_f - I_m) \cdot \hat{\beta}$ . With a close examination of the areas pointed out by the red arrows, we notice that there is certain mis-alignment, indicating that for some non-resection areas the spatial deformation does not converge to an accurate registration. This part of image profile difference, is in turn captured by intensity

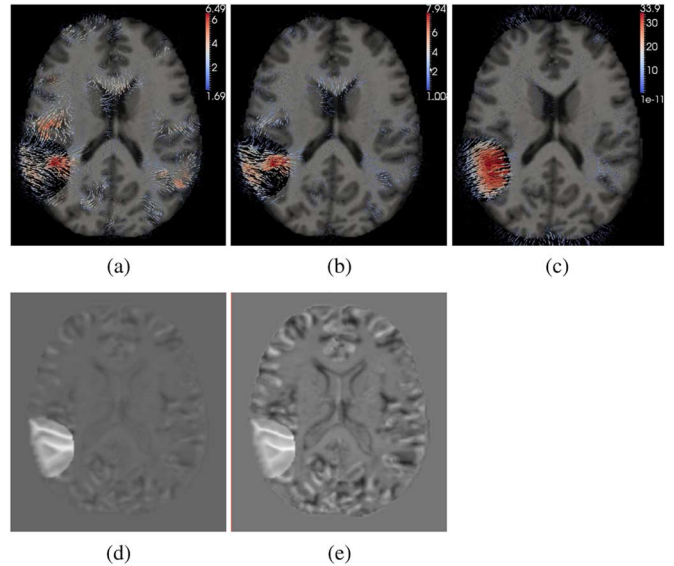


Fig. 8. Spatial and intensity deformation between old and resectioned. The upper row shows glyph plots of spatial deformation: (a) The result of REM registration with  $\beta$  function. (b) The result of REM registration with  $\hat{\beta}$  and (c) the deformation field obtained using diffeomorphic demons. The middle row shows intensity deformations: (d) corresponds to (a), the intensity deformation mostly happens to the resection area; (e) corresponds to (b), where a relatively strong intensity change happens to the entire brain.

deformation. Finally, Diffeomorphic demons is also used to register old to resectioned, with the same set of parameters as used before. The fourth row of Fig. 7 gives the checkerboard image of the result. As expected, the moving images is severely deformed around the resection area.

The residuals of the original images and registered ones are again plotted as bars (bar 4 to bar 8) in Fig. 5. Bar 4 represents the  $L_2$  image residual between old and resectioned. The residual is large, which is a mixture of the image profile change caused by resection and the structural difference between the young and old brain. Bar 5 is the image residual between young and resectioned, which equals to the value difference between bar 4 and bar 1. Bar 6 and 7 plot the image residuals after *only* applying the spatial deformation obtained using REM to the moving image, when  $\beta$  and  $\hat{\beta}$  are used, respectively. We notice that bar 6 roughly equals to the summation of bar 5 and bar 2, which is one evidence that the nonresection areas are well registered as in the case without the resection. Bar 7 shows a larger residual than bar 6, which agrees with our observation in Fig. 7 that with  $\hat{\beta}$ , the nonresection area does not converge to an accurate registration. Finally, Bar 8 plots the image residual after diffeomorphic demons registration, we see that the residual in this case is even smaller than the image profile change caused by resection, i.e., bar 8 is even shorter than bar 5. This clearly demonstrates the existence of false deformation in the result of diffeomorphic demons.

To further visualize the experiment results, in the upper row of Fig. 8, we use glyph plots to compare the deformation fields in the above experiment. Fig. 8(a) shows the result of REM registration with  $\beta$  function. We see that the deformation field on the nonresection areas appears to be very similar as in the left subfigure in Fig. 6. The region with resection still carries some

deformation energy, which is basically the accumulation of the energy dispersed from its spatial neighborhood. Fig. 8(b) shows the result of REM registration with  $\beta$ , we notice that there exists abnormally increased deformation energy around the area with resection, which is in fact false deformation. Fig. 8(c) shows the deformation field obtained using diffeomorphic demons. Note that this vector field has to be plotted in a much larger scale, where we see a severe concentration of false deformation energy around the resection area. In the corresponding columns of the lower row in Fig. 8, the intensity deformations of the two REM registration experiments are plotted. When  $\beta$  function is used, despite that we can still observe a very weak intensity change in the nonresection brain regions, which may be caused by local intensity histogram mismatch and the smoothing effect along edges of intensity change, the intensity deformation mainly occurs at the resection area. In contrast, with  $\hat{\beta}$  being used, beside the resection area, a strong intensity change happens to the entire brain, which explains the observed misalignment after applying the spatial deformation only.

### B. Registering Template to Brain MRIs With Lesions

In the first set of experiments, we registered a brain template to a set of 20 brain MR images containing white matter lesions. The moving image is a template constructed for one of our early studies [39], and was obtained by unbiased aligning and averaging a set of 130 MR images for healthy elderly subjects (age > 58) from the OASIS dataset [40]. The testing set of 20 brain MR images with lesions were also from OASIS dataset, but none of them were used in the template construction.

The template is affinely registered to the fixed images before applying our deformable registration algorithm. Compared to MR images of individual subjects, brain templates are smooth. As a result, in the experiments, we used small Gaussian Kernels for the smoothing of deformation fields:  $\sigma_{\text{fluid}} = \sigma_{\text{diff}} = 0.8$  for  $K_{\text{fluid}}$  and  $K_{\text{diff}}$ , respectively. Lesions were segmented using the FreeSurfer tool [41] (segmented with the label *white matter hypointensity lesion*), and  $\beta$  was constructed with  $\sigma_{\text{prob}} = 1$  for  $K_{\text{prob}}$  in (15);  $\epsilon = 0.01$  in (7) and  $\sigma_{\text{int}} = 0.4$  for  $K_{\text{int}}$ . In all of the 20 registration experiments, the image residual stopped dropping and began oscillating within 15–25 iterations, so we terminated all registrations at the 30th iteration. Sample curves plotting the registration residual during the registration process for one of the experiments are shown in Fig. 9(a), where the solid line plots the image  $L_2$  residual after the spatial deformation field of the current iteration is applied to the moving image, and the dashed line plots the image  $L_2$  residual after the intensity displacement is *additionally* applied. From these curves, we observe a smooth diffusion process both on the evolution of spatial deformation and on that of the intensity displacement. The image  $L_2$  residuals before and after the registration for all the 20 experiments are shown in Fig. 9(b). The blue bar shows the  $L_2$  residual between the moving and the fixed images before applying our deformable registration. The red bar shows the  $L_2$  residual between the spatially-deformed moving image and the fixed image, where we can see a significant drop of residual values compared to the corresponding blue bar. We also observe a further drop of residual values on the green bars, which are the

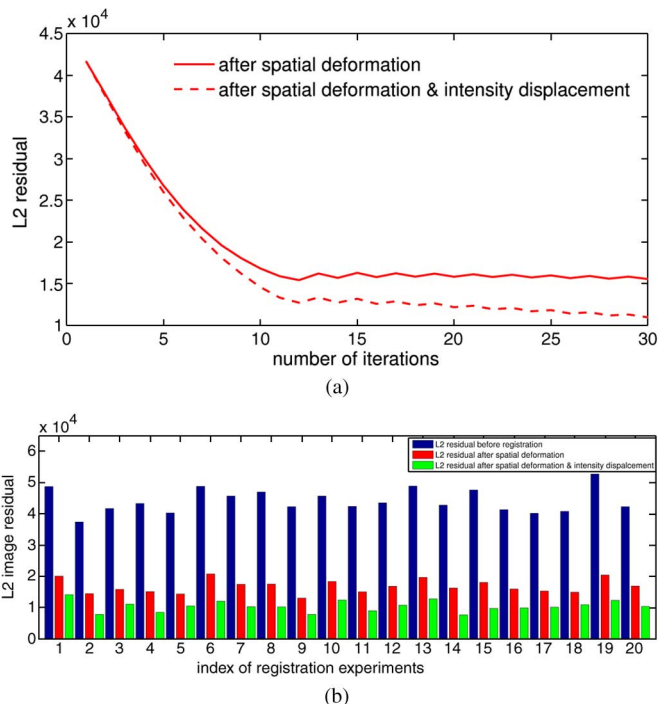


Fig. 9. (a) Sample curves plotting the registration residual during the registration process. The solid line plots the image  $L_2$  residual after the spatial deformation field of the current iteration is applied to the moving image, and the dashed line plots the image  $L_2$  residual when the intensity displacement is additionally applied. (b) Image  $L_2$  residuals before and after registration. The blue bars show the  $L_2$  residuals between the moving and the fixed images before the deformable registration. The red bars show the  $L_2$  residuals between the spatially deformed moving image and the fixed images. The green bars show the  $L_2$  residuals after the intensity displacement is further applied to the fixed image.

$L_2$  residuals after the intensity displacement is applied to the fixed image, in addition to spatial deformation. In other words, the green bar shows the registration residual after removing the contribution from the intensity difference caused by topological change.

A sample of the registration results is given in Fig. 10. The first row of Fig. 10 shows the checkerboard image of the template and the fixed image. The second row shows the checkerboard image of the fixed image and the registered template, i.e., after spatial deformation. The fixed image that contains lesions is given in the third row, where the segmentation result using the FreeSurfer are marked out using blue contours. The fourth row gives the fixed images after intensity displacement is applied. The three columns in Fig. 10 show the axial, sagittal, and coronal views, respectively. By examining the areas pointed out by red arrows, we see that the anatomical structures of the template are well aligned with those on the fixed images and the intensity within lesions in the fixed image is corrected to that of healthy white matter.

Fig. 11 provides some samples of the resulting deformation vector fields using a glyph view. The template image (the leftmost column) was registered to two subjects with severe lesions (the second column). After the registration, the template image is deformed to align with the subjects, as shown in the third column. In the last column, we show a zoom-in view where the deformation fields are plotted as glyph fields on top of the fixed image. For the first subject (the upper row), we focus on the lesions around the first ventricle, and for the second subject (the

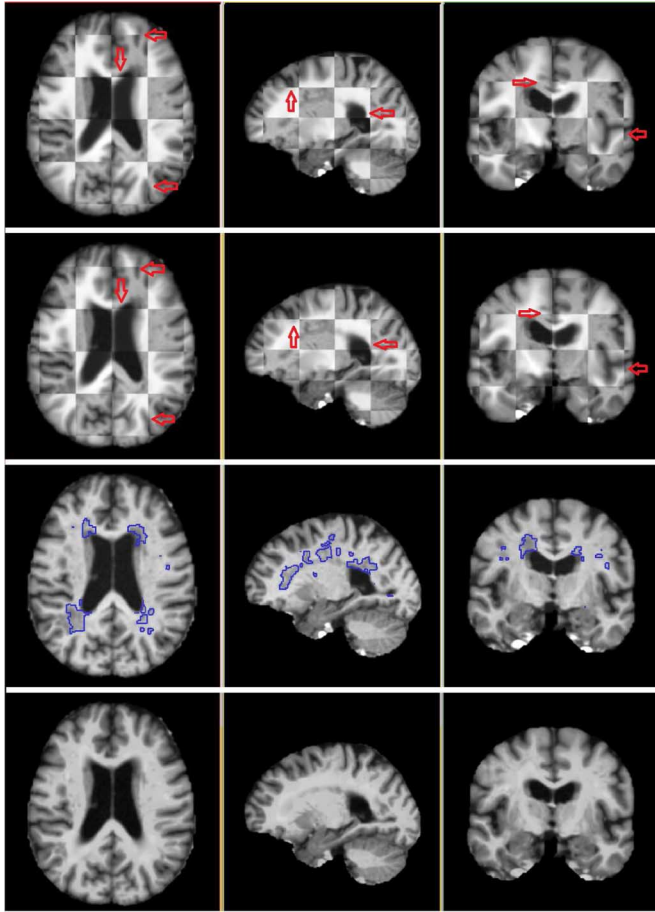


Fig. 10. Sample of registration results from a template to a subject with lesion from OASIS dataset. The first row shows the checkerboard image of the template and the fixed image. The second row shows the checkerboard image of the fixed image and the registered template, i.e., after spatial deformation. The third row shows the fixed image that carries lesions, which are marked out by blue contours. The fourth row gives the fixed image after intensity displacement is applied. The columns are for the axial, sagittal, and coronal views of each volume, from left to right, respectively.

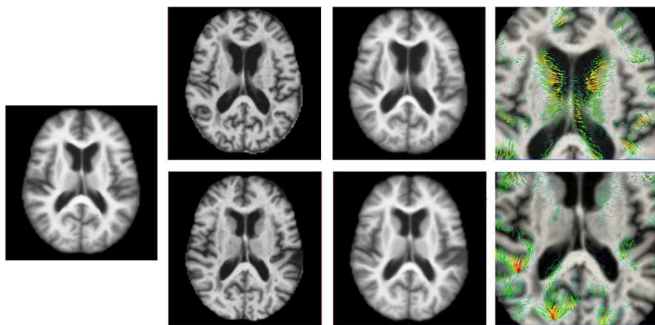


Fig. 11. Samples of the resulting deformation vector fields from a template to subjects with lesion from OASIS dataset. Vector fields are shown in glyph views. Left-most column: the template image. Second column from left: two subjects with severe lesions. Third column from left: the spatially deformed template image after registration. Right-most column: zoom-in view of the deformation fields on top of the fixed image. For the first subject (upper row), zoom-in view focusing on the lesions around the first ventricle. For the second subject (lower row), zoom-in view focusing on the lesion around the lateral ventricle.

lower row), we focus on the lesion around the lateral ventricle. From both cases, we found no false deformation around the lesion areas.

### C. Registering Brain MRIs of Healthy Subject to Those of Alzheimer's Patients

In this set of experiments, we registered an old subject (the same one used in Section IV-A) to a set of 20 brain MR images with lesions in the ADNI dataset.<sup>5</sup> The images from ADNI dataset were skull-stripped using the FSL (BET) tool [42].

In these experiments, because we were conducting subject-to-subject registration, the moving image had lower SNR and was sharper compared to the template image used in Section IV-A. As a result, we used larger Gaussian kernels for the smoothing of deformation fields, compared with those used in the previous set of experiments. Specifically, we used  $\sigma_{\text{fluid}} = \sigma_{\text{diff}} = 1.2$  for  $K_{\text{fluid}}$  and  $K_{\text{diff}}$ , respectively. Other parameters were:  $\sigma_{\text{prob}} = 1$  for  $K_{\text{prob}}$  in (15);  $\epsilon = 0.02$  in (7) and  $\sigma_{\text{int}} = 0.4$  for  $K_{\text{int}}$ . In the registration experiments, the moving image was first affinely registered to the fixed images. During registration the image residual stopped dropping and started oscillating after 50–80 iterations, so we terminated the registration for all experiments at 100 iterations. Sample curves plotting the registration residual during the registration process for one of the experiments are shown in Fig. 12(a), with the same configuration as that used in Fig. 9(a). The image  $L_2$  residuals before and after the registration for all the 20 experiments are shown in Fig. 12(b), in the same fashion as in Fig. 9(b). A sample of registration results is given in Fig. 13, which is organized in the same fashion as in Fig. 10. We can see that the moving image are spatially deformed and well aligned with the fixed image, and the lesions in the fixed images are corrected to the appearance of healthy white matter after the intensity displacement is applied.

Again, we used diffeomorphic demons algorithm [32] to perform the same set of registration experiments as comparison. Three resolutions are used in the diffeomorphic demons registration, and 50, 50, and 200 iterations were performed in each resolution, respectively. The variances used in the smoothing Gaussian kernel for fluid and diffusion regularization are both set to 1.2, the same as in our algorithm. In Fig. 12(b), in addition to the residuals plotted as in Fig. 12(a), the magenta bars show the registration residual after applying the diffeomorphic demons registration. We can see that in all the cases, the residuals after applying diffeomorphic demons have values in between the residuals before and after the intensity displacements (the red and green bars, respectively). Intuitively, in diffeomorphic demons, part of the spatial deformation attempted to minimize the error caused by the intensity difference of the lesions. This in turn caused false deformation.

Now we demonstrate the efficacy of our algorithm in eliminating false deformation. Fig. 14(a) and (b) shows the registration

<sup>5</sup>Data used in this paper are selected from the Alzheimer's disease Neuroimaging Initiative (ADNI) database (<http://www.loni.ucla.edu/ADNI>). The ADNI was launched in 2003 by the National Institute on Aging (NIA), the National Institute of Biomedical Imaging and Bioengineering (NIBIB), the Food and Drug Administration (FDA), private pharmaceutical companies and non-profit organizations, as a \$60 million, five-year public-private partnership. The primary goal of ADNI has been to test whether serial magnetic resonance imaging (MRI), positron emission tomography (PET), other biological markers, and clinical and neuropsychological assessment can be combined to measure the progression of mild cognitive impairment (MCI) and early Alzheimer's disease (AD). Determination of sensitive and specific markers of very early AD progression is intended to aid researchers and clinicians to develop new treatments and monitor their effectiveness, as well as lessen the time and cost of clinical trials.

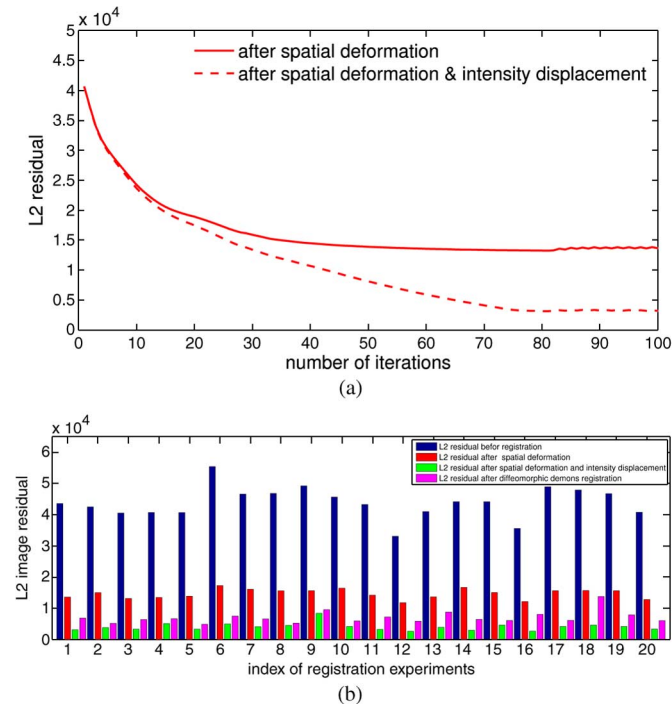


Fig. 12. (a) Sample curves plotting the registration residual during the registration process. (b) Image  $L_2$  residuals before and after registration. Figure plotted in the same fashion as in Fig.~9. In addition, the magenta bars show the  $L_2$  residual after applying diffeomorphic demons registration.

results using our proposed algorithm and diffeomorphic demons. In both (a) and (b), the subfigures in the upper rows, from left to right, show axial views of the moving image, the fixed image, the registered moving image (after spatial deformation) using our algorithm, and the registered moving image (after spatial deformation) using diffeomorphic demons. In both cases, we find that the diffeomorphic demons algorithm tries to deform the lateral ventricle into the white matter areas with lesions, which leads to an incorrect registration result. In contrast, these errors are not seen in our registration results. Furthermore, in both (a) and (b), the left most subfigure in the lower row shows a zoomed region in order to visualize the deformation field. The second and third subfigures in both lower rows of (a) and (b) give the glyph views of the deformation field obtained using our method and diffeomorphic demons, respectively. For diffeomorphic demons, we can observe a dense deformation energy concentration (abnormally long vectors) around the lesion-affected areas in the resulting deformation field, which is obviously false deformation. On the other hand, such false deformation is successfully removed in the results obtained using our algorithm. We need to point out that, despite the advantages of our algorithm shown by these results, keep in mind that our algorithm does take lesion segmentation as an additional input which is important prior knowledge.

#### D. Impact of False Alarm and Mis-Detection of Lesions

To eliminate false deformation, our registration method relies on an *a priori* lesion estimation. However, the lesion segmentation obtained from automatic segmentation tools is imperfect. Here, we provide some examples to demonstrate the impact these errors have on our algorithm.

As explained in Section III-B,  $\beta$  is a function of a smoothed lesion segmentation. Fig. 15 shows such a case in our second

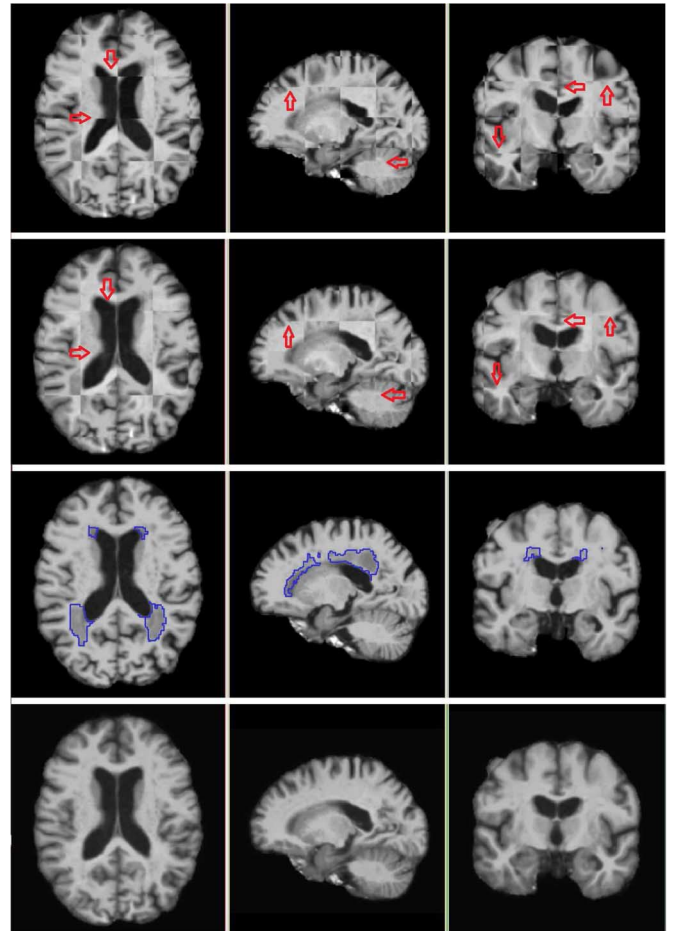


Fig. 13. Sample of registration results from the image of a healthy subject from OASIS dataset to an image with lesion from ADNI dataset. The first row shows the checkerboard image of the template and the fixed image. The second row shows the checkerboard image of the fixed image and the registered template, i.e., after spatial deformation. The third row shows the fixed image that carry lesions, which are marked out by blue contours. The fourth row gives the fixed image after intensity displacement is applied. The columns represent the axial, sagittal, and coronal views of each volume, from left to right, respectively.

set of experiments (Section IV-B). From Fig. 15(a), we notice that FreeSurfer underestimated the lesion-affected areas (inside the blue contours), especially the lesion region to the left of the ventricle. Fig. 15(b) shows the smoothing effect of the constructed  $p(x, y, z)$  function. All the lesions in the fixed image are successfully removed after intensity displacement, as shown in Fig. 15(c). Finally, in Fig. 15(d), we can see that the deformation field was not affected by the presence of lesions, i.e., no false deformation was observed. This result demonstrated that slightly over- or under-segmentation is tolerated by our algorithm.

However, if a lesion-affected area is completely mis-detected, the registration performance will be affected. An example is shown in Fig. 16(a), which gives the coronal view of a moving image, a fixed image, and a registered moving image after applying the spatial deformation, from left to right, respectively. We find that the skull stripping of the fixed image obtained by FSL (BET) is not perfect, and some extracranial tissue was kept as part of the brain. This tissue does not have matching anatomy in the moving image, and thus, it can be regarded as a topological change. In fact, such errors are commonly seen in large scale

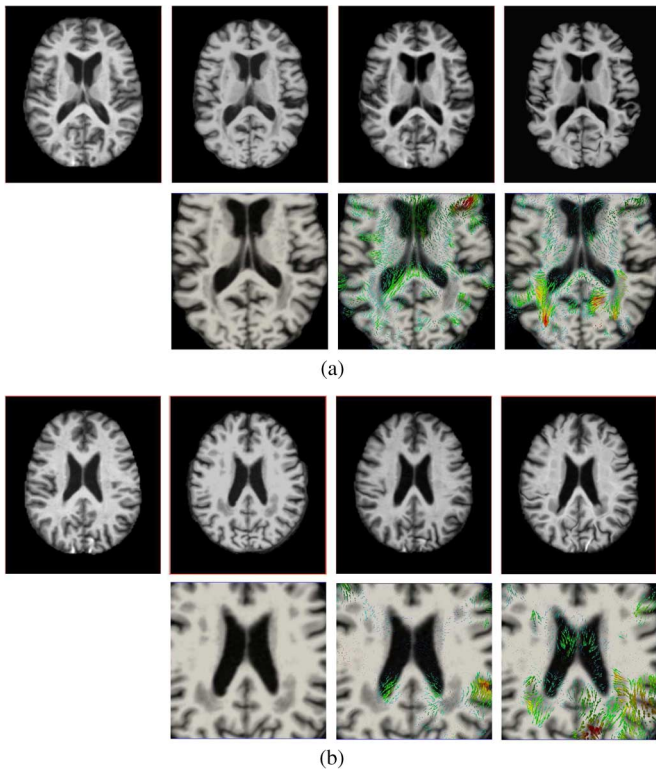


Fig. 14. Comparison of our algorithm with diffeomorphic demons by registering a healthy subject from OASIS dataset to images with lesion from ADNI dataset. In both (a) and (b), the subfigures in the upper row, from left to right, show an axial view of the moving image, the fixed image, the registered moving image (after spatial deformation) using our algorithm, and the registered moving image (after spatial deformation) using diffeomorphic demons. Also, in both (a) and (b), the left most subfigure in the lower row indicates a region that we zoom-in to visualize the deformation field. The second and third subfigures from the left gives the glyph view of the deformation field obtained using our method and diffeomorphic demons, respectively.

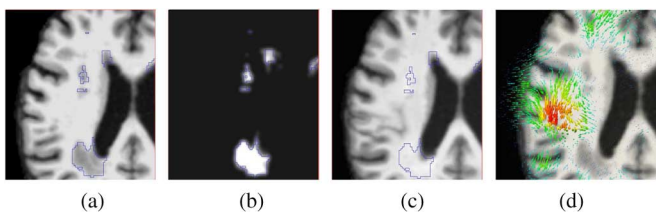


Fig. 15. Impact of imperfect lesion segmentation on our registration algorithm. (a) Lesion segmentation obtained using FreeSurfer, lesion areas are underestimated and marked out using blue contours. (b) The constructed  $\beta$  function. (c) Result after intensity displacement applied to the fixed image. (d) the deformation field.

studies. Fig. 16(b) shows the deformation field around this area, where we observe some false deformation. Ideally, if this area was modeled in  $\beta$ , it will be corrected by intensity displacement and should not cause any spatial deformation.

Underestimation or even misdetection is common in automatic lesion segmentation algorithms, due to the minor intensity differences of some lesions. However, it is relatively uncommon to see false alarms during lesion detection, since it is expected that there always exist some intensity difference. Thus, in the two sets of experiments, we do not have results to show the impact of false alarm. However, it is reasonable to expect that if

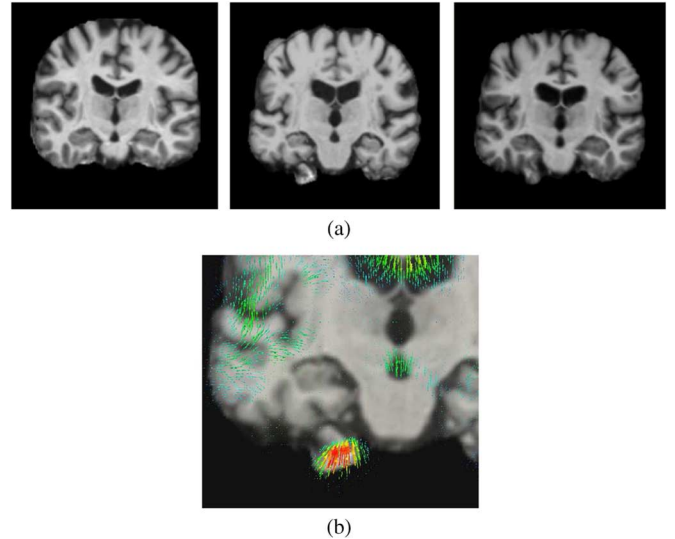


Fig. 16. Impact of misdetection of topological change on the registration result. (a) From left to right: coronal view of the moving image, fixed image, registered moving image, i.e., after spatial deformation. (b) False deformation caused by the misdetection of topological change.

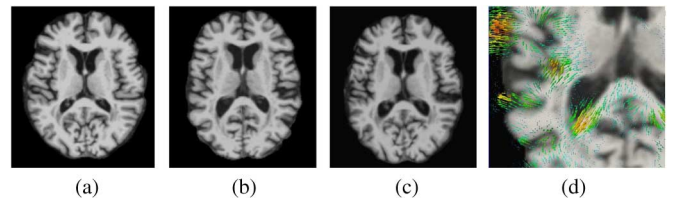


Fig. 17. Sample registration when both moving and fixed image carry lesion. (a) Moving image with lesion. (b) Fixed image with lesion. (c) Deformed moving image after spatial deformation. (d) The deformation field.

false alarm happens to regions with no or minor intensity difference between the moving and the fixed images, our registration algorithm would perform normally. The reason is that if the intensity of certain region on the moving and the fixed images are very close,  $\phi$  will have small values for these regions and no spatial deformation or intensity displacement will be exerted, even though  $p(x, y, z)$  has large values. On the other hand, if the region of false alarm covers mis-aligned boundaries between the moving and the fixed images, the deformation energy will be concentrated on intensity deformation.

Finally, we point out that the current version of our algorithm only deals with lesions in the fixed image and a normal anatomical topology of the moving image is required. Fig. 17 shows the registration results when both the moving image [Fig. 17(a)] and the fixed image [Fig. 17(b)] have lesions (from the ADNI dataset). Only the lesion segmentation for the fixed image is modeled in  $\beta$ . We observed that around the left side of lateral ventricle, the deformed moving image [Fig. 17(c)] is not well aligned with the fixed image after registration, and false deformation is present, as shown in Fig. 17(d).

#### E. Register Template to a Brain Image With a Tumor

In this experiment, we registered a brain MR image template, as shown in the first row of Fig. 18, to a fixed image that carries a brain tumor of considerable size, as shown in the second row of

Fig. 18.<sup>6</sup> The template image was constructed using 233 healthy young subjects (mean age  $\approx 35$ ) from OASIS dataset in our previous study [39]. The subject brain image with a meningioma was obtained from the testing data distributed within the Slicer3 [43] package. It was skull-stripped using the FSL (BET) tool [42]. As shown in the second row of Fig. 18, instead of a precise segmentation of the tumor, our interface allowed a physician to draw 3 profile lines on the fixed image to indicate the location and size of the tumor (with orange line), which gives us an ellipsoid containing the tumor region (blue contours).

The registration process and results are shown in Fig. 18. Due to the large size of the topological change, we use a large Gaussian kernel for  $p(x, y, z)$ ,  $\sigma_{\text{prob}} = 4$  for  $K_{\text{prob}}$  in (15), and all the other parameters are set to the same as in Section IV-B. The third row of Fig. 18 gives the checkerboard image of the fixed image and the template; where the fourth row gives the checkerboard image of the fixed images and the registered template, after applying spatial deformation. We find that after registration, the template is well aligned with the fixed image. The fifth row shows the fixed image after applying intensity displacement, where we see the intensity of the tumor region is corrected by that of the co-aligned template image. This step essentially provides us with a “tumor-repaired” version of the fixed image, which is an estimation of the brain anatomy had the tumor not existed. We notice that in the fixed image, the growth of tumor pushes the surrounding tissue aside and squeezes the ventricle. After intensity correction, the healthy tissue is moved back to the normal location and the ventricle is lifted. In Fig. 19, we plot the resulting deformation field using glyphs. Clearly, the tumor does not induce local deformation, despite the strong intensity gradient between the tumor region and the surrounding healthy tissue.

#### F. Impact of Diffeomorphic Constraint

In this section, we conduct an experiment to demonstrate the impact as well as the importance of the diffeomorphic constraint. In Fig. 20, we show the resulting deformation field when the experiment in Fig. 13 is conducted with the exact same set of parameters, except that we replace the deformation updating rule given in step 3 of REM registration algorithm with the following:

3) update deformation field:  $s \leftarrow s + u$ ,

i.e., we remove the diffeomorphic constraint by replacing the intrinsic updating rule with a simple additive updating. In these plots, we keep the original scale of the glyph lengths in voxel unit. A zoom-in view is given in the right figure, where we can observe that regions with the head of glyphs overlap, as pointed

<sup>6</sup>Note that in the second row and in the checkerboard images in the third and fourth rows, the fixed image appears to be much darker compared to the template. The appearances of the fixed image before and after intensity correction, as shown in the second and fifth rows, are also very different. This is due to the fact that the fixed image has a very different intensity profile because of the bright tumor. As a result, the contrast of the whole image is not good, where CSF appears to be dark and not really visible. However, if we pay some close attention, it is easy to notice that major features, such as the separation between gray matter and white matter and the boundary of ventricle are all well aligned after the deformable registration. Also, as shown in the fifth row, after the intensity of the tumor region is repaired, brain regions other than the tumor can be visualized with a proper intensity contrast.

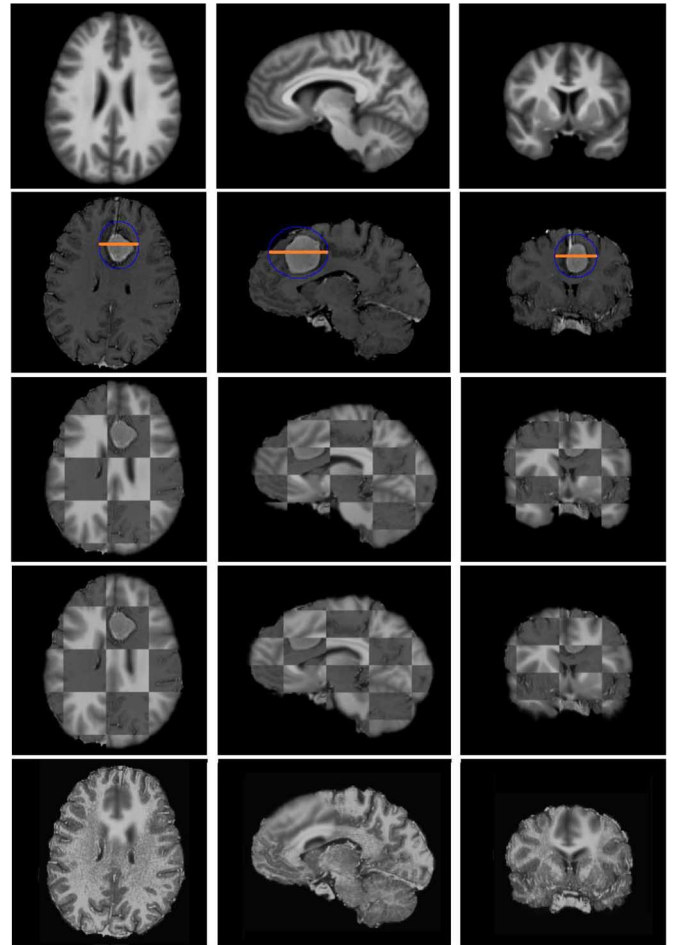


Fig. 18. Sample registration of a brain template to the MRI of a meningioma patient. First row: a brain template, the moving image. Second row: fixed image, MRI of a meningioma patient. The blue ellipsoid marks out the tumor region. Third and fourth row: checkerboard image of the fixed and the moving image, before and after spatial deformation, respectively. The fifth row: the intensity corrected fixed image after intensity displacement. The three columns show the axial, sagittal, and coronal views of the same image.

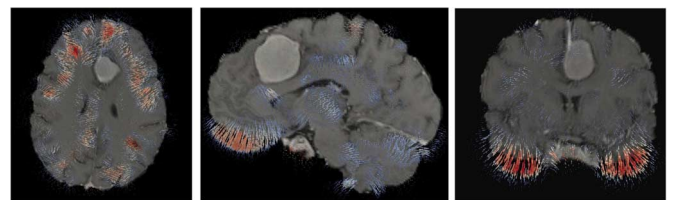


Fig. 19. Deformation field of registering a brain template to the MRI of a meningioma patient in glyph plot. The three columns give the axial, sagittal, and coronal views of the same image, respectively.

out by the yellow arrows. The overlapping means that there exists flipped ordering of adjacent voxel after the deformation.

An important property of diffeomorphism is its invertibility, which means if we have a diffeomorphism that maps the moving image to the image space of the fixed image, it can be uniquely inverted to map the fixed image to the image space of the moving image. The inverse of a diffeomorphism can be robust and efficiently computed by many existing methods, such as describe in [44]. In our algorithm, we intentionally set the image with topological change as the fixed image to avoid the additional warping of the  $\beta$  function in each iteration, which considerably decreased the computational load. However, in clinical applications, there are many cases when images of individual patients need to be

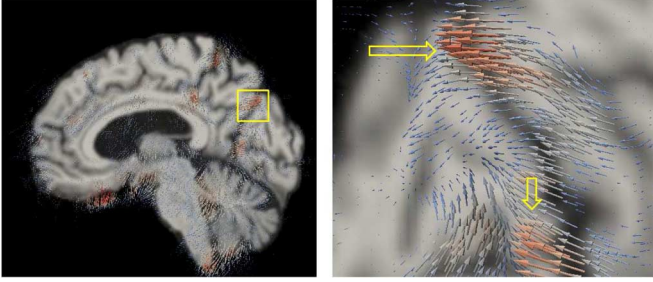


Fig. 20. Resulting deformation field when diffeomorphic constraint is turned off. Scale of the glyph lengths is in actual voxel unit. Right figure is a zoom-in view of the marked out region in the deformation field shown by the left subfigure.

mapped into the image space of a common template. The invertibility of diffeomorphism enables the application of our algorithm in these cases. To illustrate this, we used the tool developed by Luethi *et al.* [45] to invert the deformation fields shown in Figs. 13 and 18. Fig. 21(a) shows the result corresponding to Fig. 13, where the first row shows the healthy subject, the second row shows the image with topological change and the third row shows result when the images with topological changes is mapped to the image space of the healthy subject. Similar result corresponding to Fig. 18 is given in Fig. 21(b), where the third row shows the result when the image with tumor is mapped to the template image space.

## V. CONCLUSION AND FUTURE WORK

In this work, we present a new deformable registration algorithm for images with topological changes. The proposed algorithm is capable of incorporating a segmentation as an additional input and eliminating false deformation in the resulting deformation field. The registration is performed by embedding images in  $\mathbb{R}^3$  Euclidian space into surfaces in an  $\mathbb{R}^4$  Riemannian space. Then the image registration is modeled as a surface evolution process. The proposed algorithm was extensively tested on different brain MR image datasets carrying minor to severe pathology. The registration results are compared with those obtained from diffeomorphic demons, which demonstrate the efficacy of our proposed algorithm in terms of converging to correct registration in the presence of lesion.

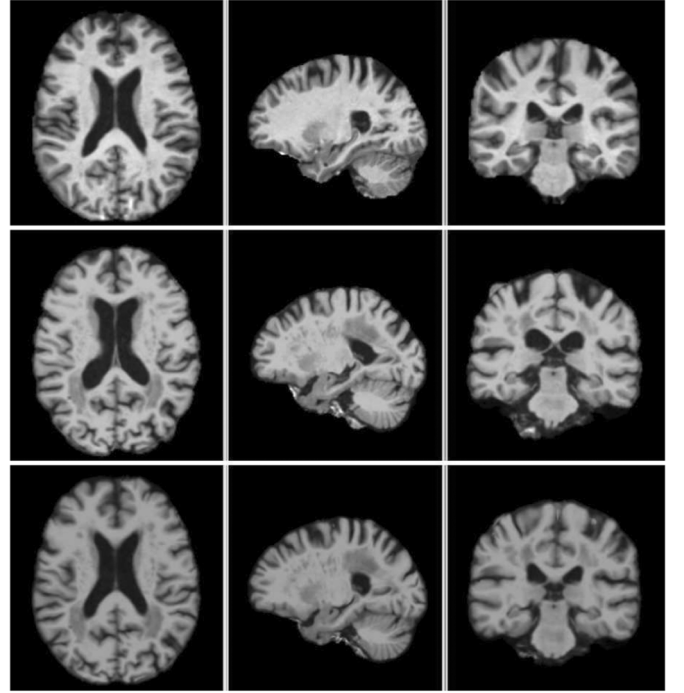
The current version of our implementation only allows the fixed image to contain lesion. A direct extension would be to symmetrize the energy function and allow lesions present in both the moving and the fixed images to be modeled by separate probability maps. Other potential improvements include a multiscale implementation and more automated stopping criteria. Mutual information might also be used instead of the  $L_2$  image residual in the embedding function  $\phi$ , which will further allow our proposed algorithm to register images across different modalities.

## APPENDIX

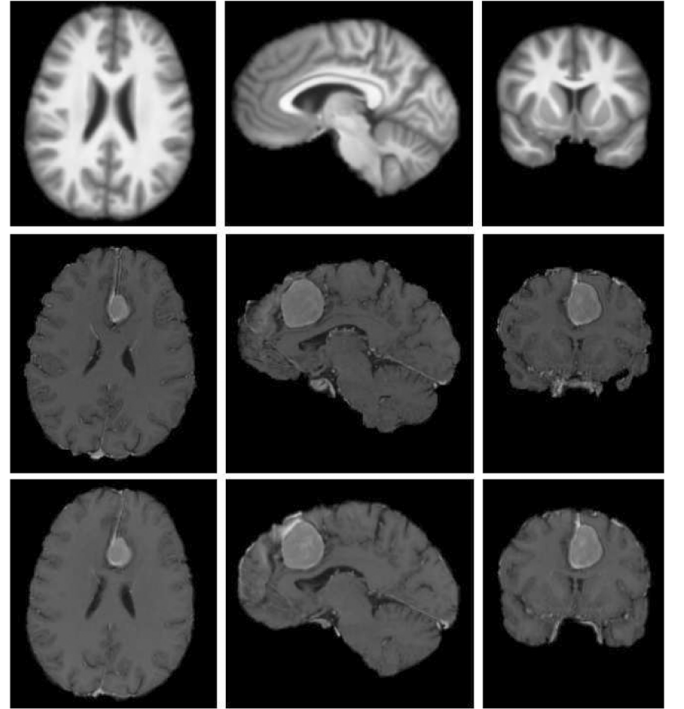
From (6), we get

$$h^{-1} = \begin{bmatrix} \frac{1}{\phi} & 0 & 0 & 0 \\ 0 & \frac{1}{\phi} & 0 & 0 \\ 0 & 0 & \frac{1}{\phi} & 0 \\ 0 & 0 & 0 & \frac{1}{\beta\phi} \end{bmatrix}. \quad (19)$$

Thus, we can compute the Levi-Civita connections using (5) (see (20)–(23) on the next page). The inverse of the metric  $g$



(a)



(b)

Fig. 21. Invertibility of diffeomorphism. (a) The result corresponding to Fig. 13, where the first row shows the healthy subject, the second row shows the image with topological change and the third row shows result when the images with topological changes is mapped to the image space of the healthy subject. (b) Shows a similar result corresponding to Fig. 18, where the third row shows the result when the image with tumor is mapped to the template image space.

has the following form:

$$g^{-1} = \frac{\begin{bmatrix} 1 + \beta I_y^2 + \beta I_z^2 & -\beta I_x I_y & -\beta I_x I_z \\ -\beta I_x I_y & 1 + \beta I_x^2 + \beta I_z^2 & -\beta I_y I_z \\ -\beta I_x I_z & -\beta I_x I_z & 1 + \beta I_x^2 + \beta I_y^2 \end{bmatrix}}{\phi (1 + \beta I_x^2 + \beta I_y^2 + \beta I_z^2)}. \quad (24)$$

Plug all the above terms into the Euler-Lagrange equation in (4), we get the first equation shown on the next page.

Then  $\partial X^2/\partial t$  and  $\partial X^3/\partial t$  can be obtained in the symmetric forms. And after mathematical manipulations,  $\partial X^4/\partial t$  can be derived as shown in the second equation on the bottom of page.

$$\Gamma^1 = \frac{1}{2\phi} \begin{bmatrix} \phi_x & \phi_y & \phi_z & \phi_I \\ \phi_y & -\phi_x & 0 & 0 \\ \phi_z & 0 & -\phi_x & 0 \\ \phi_I & 0 & 0 & -(\beta\phi_x + \beta_x\phi) \end{bmatrix} \quad (20)$$

$$\Gamma^2 = \frac{1}{2\phi} \begin{bmatrix} -\phi_y & \phi_x & 0 & 0 \\ \phi_x & \phi_y & \phi_z & \phi_I \\ 0 & \phi_z & -\phi_y & 0 \\ 0 & \phi_I & 0 & -(\beta\phi_y + \beta_y\phi) \end{bmatrix} \quad (21)$$

$$\Gamma^3 = \frac{1}{2\phi} \begin{bmatrix} -\phi_z & 0 & \phi_x & 0 \\ 0 & -\phi_z & \phi_y & 0 \\ \phi_x & \phi_y & \phi_z & \phi_I \\ 0 & 0 & \phi_I & -(\beta\phi_z + \beta_z\phi) \end{bmatrix} \quad (22)$$

$$\Gamma^4 = \frac{1}{2\beta\phi} \begin{bmatrix} -\phi_I & 0 & 0 & \beta\phi_x + \beta_x\phi \\ 0 & -\phi_I & 0 & \beta\phi_y + \beta_y\phi \\ 0 & 0 & -\phi_I & \beta\phi_z + \beta_z\phi \\ \beta\phi_x + \beta_x\phi & \beta\phi_y + \beta_y\phi & \beta\phi_z + \beta_z\phi & \beta\phi_I \end{bmatrix}. \quad (23)$$

$$\begin{aligned} \frac{\partial X^1}{\partial t} &= \frac{\phi^2}{\sqrt{g}} \partial_\mu (\sqrt{g} g^{\mu\nu} \partial_\nu X^1) + \phi^2 \Gamma_{jk}^1 \partial_\mu X^j \partial_\nu X^k g^{\mu\nu} \\ &= \frac{\phi^2}{\sqrt{g}} [\partial_x (\sqrt{g} g^{11}) + \partial_y (\sqrt{g} g^{21}) + \partial_z (\sqrt{g} g^{31})] \\ &\quad + \phi^2 (\Gamma_{11}^1 g^{11} + 2\Gamma_{12}^1 g^{12} + 2\Gamma_{13}^1 g^{13}) \\ &\quad + 2\phi^2 \Gamma_{14}^1 (I_x g^{11} + I_y g^{12} + I_z g^{13} + \Gamma_{22}^1 g^{22} + \Gamma_{33}^1 g^{33}) \\ &= - \frac{\phi\beta I_x [(1 + \beta I_y^2 + \beta I_z^2) I_{xx} + (1 + \beta I_x^2 + \beta I_z^2) I_{yy} + (1 + \beta I_x^2 + \beta I_y^2) I_{zz}]}{(\beta I_x^2 + \beta I_y^2 + \beta I_z^2 + 1)^2} \\ &\quad + \frac{2\phi\beta^2 I_x (I_x I_y I_{xy} + I_x I_z I_{xz} + I_y I_z I_{yz})}{(\beta I_x^2 + \beta I_y^2 + \beta I_z^2 + 1)^2} \\ &\quad - \frac{3I_x (\phi_x \beta I_x + \phi_y \beta I_y + \phi_z \beta I_z - \phi_I) - 2\phi_I I_x}{2(1 + \beta I_x^2 + \beta I_y^2 + \beta I_z^2)} \\ &\quad - \frac{\phi I_x (2 + \beta I_x^2 + \beta I_y^2 + \beta I_z^2) (\beta_x I_x + \beta_y I_y + \beta_z I_z)}{2(1 + \beta I_x^2 + \beta I_y^2 + \beta I_z^2)^2} \end{aligned}$$

$$\begin{aligned} \frac{\partial X^4}{\partial t} &= \frac{\phi^2}{\sqrt{g}} \partial_\mu (\sqrt{g} g^{\mu\nu} \partial_\nu X^4) + \phi^2 \Gamma_{jk}^4 \partial_\mu X^j \partial_\nu X^k g^{\mu\nu} \\ &= \frac{\phi^2}{\sqrt{g}} [\partial_x (\sqrt{g} (g^{11} I_x + g^{12} I_y + g^{13} I_z)) + \partial_y (\sqrt{g} (g^{21} I_x + g^{22} I_y + g^{23} I_z)) \\ &\quad + \partial_z (\sqrt{g} (g^{31} I_x + g^{32} I_y + g^{33} I_z))] \\ &\quad + \Gamma_{11}^4 g^{11} + 2\Gamma_{14}^4 (I_x g^{11} + I_y g^{12} + I_z g^{13}) + 2\Gamma_{24}^4 (I_x g^{21} + I_y g^{22} + I_z g^{23}) \\ &= \frac{\phi [(1 + \beta I_y^2 + \beta I_z^2) I_{xx} + (1 + \beta I_x^2 + \beta I_z^2) I_{yy} + (1 + \beta I_x^2 + \beta I_y^2) I_{zz}]}{(1 + \beta I_x^2 + \beta I_y^2 + \beta I_z^2)^2} \\ &\quad - \frac{2\phi\beta I_x (I_x I_y I_{xy} + I_x I_z I_{xz} + I_y I_z I_{yz})}{(1 + \beta I_x^2 + \beta I_y^2 + \beta I_z^2)^2} \\ &\quad + \frac{3(\phi_x \beta I_x + \phi_y \beta I_y + \phi_z \beta I_z - \phi_I) - \phi_I (\beta I_x^2 + \beta I_y^2 + \beta I_z^2)}{2\beta (1 + \beta I_x^2 + \beta I_y^2 + \beta I_z^2)} \\ &\quad + \frac{\phi (\beta_x I_x + \beta_y I_y + \beta_z I_z) (2 + \beta I_x^2 + \beta I_y^2 + \beta I_z^2)}{2\beta (1 + \beta I_x^2 + \beta I_y^2 + \beta I_z^2)^2} \end{aligned}$$

## ACKNOWLEDGMENT

The authors would like to thank the Associate Editor and anonymous reviewers for pointing out some related work to complete the literature review and providing valuable suggestions to improve the quality of the paper.

## REFERENCES

- [1] U. Grenander and M. I. Miller, "Computational anatomy: An emerging discipline," *Q. Appl. Math.*, no. 4, pp. 617–695, 1998.
- [2] J. Ashburner and K. J. Friston, "Voxel-based morphometry—the methods," *NeuroImage*, vol. 11, no. 6, pp. 805–821, 2000.
- [3] C. D. Good, I. S. Johnsrude, J. Ashburner, R. N. Henson, K. J. Friston, and R. S. Frackowiak, "A voxel-based morphometric study of ageing in 465 normal adult human brains," *NeuroImage*, vol. 14, no. 1, pp. 21–36, 2001.
- [4] C. Davatzikos, A. Genc, D. Xu, and S. M. Resnick, "Voxel-based morphometry using the RAVENS maps: Methods and validation using simulated longitudinal atrophy," *NeuroImage*, vol. 14, no. 6, pp. 1361–1369, 2001.
- [5] N. Lepore, C. Brun, Y. Y. Chou, M. C. Chiang, R. A. Dutton, K. M. Hayashi, E. Luders, O. L. Lopez, H. J. Aizenstein, A. W. Toga, J. T. Becker, and P. M. Thompson, "Generalized tensor-based morphometry of HIV/AIDS using multivariate statistics on deformation tensors," *IEEE Trans. Med. Imag.*, vol. 27, no. 1, pp. 129–141, Jan. 2008.
- [6] G. Gilboa, N. Sochen, and Y. Y. Zeevi, "Forward-and-backward diffusion processes for adaptive image enhancement and denoising," *IEEE Trans. Image Process.*, vol. 11, no. 7, pp. 689–703, Jul. 2002.
- [7] R. G. Boyes, J. L. Gunter, C. Frost, A. L. Janke, T. Yeatman, D. L. G. Hill, M. A. Bernstein, P. M. Thompson, M. W. Weiner, N. Schuff, G. E. Alexander, R. J. Kiliany, C. DeCarli, C. R. Jack, N. C. Fox, and A. D. N. I. Study, "Intensity non-uniformity correction using n3 on 3-t scanners with multichannel phased array coils," *Neuroimage*, vol. 39, no. 4, pp. 1752–1762, 2008.
- [8] X. Hua, A. D. Leow, N. Parikshak, S. Lee, M.-C. Chiang, A. W. Toga, C. R. Jack, M. W. Weiner, and P. M. Thompson, "Tensor-based morphometry as a neuroimaging biomarker for Alzheimer's disease: An MRI study of 676 AD, MCI, and normal subjects," *NeuroImage*, vol. 43, no. 3, pp. 458–469, 2008.
- [9] L. Pantoni and D. Inzitari, "New clinical relevance of leukoaraiosis," *Stroke*, vol. 29, no. 2, p. 543, 1998.
- [10] X. Li and C. L. Wyatt, "Modeling topological changes in deformable registration," in *Proc. 2010 IEEE Int. Conf. Biomed. Imag.*, 2010, pp. 360–363.
- [11] M. Sdika and D. Pelletier, "Nonrigid registration of multiple sclerosis brain images using lesion inpainting for morphometry or lesion mapping," *Human Brain Mapp.*, vol. 30, no. 4, pp. 1060–1067, 2009.
- [12] N. Koutsouleris, E. M. Meisenzahl, C. Davatzikos, R. Bottlender, T. Frodl, J. Scheuerecker, G. Schmitt, T. Zetzsche, P. Decker, M. Reiser, H.-J. Möller, and C. Gaser, "Use of neuroanatomical pattern classification to identify subjects in at-risk mental states of psychosis and predict disease transition," *Arch. General Psychiatry*, vol. 66, no. 7, pp. 700–712, 2009.
- [13] S. M. Andersen, S. Z. Rapcsak, and P. M. Beeson, "Cost function masking during normalization of brains with focal lesions: Still a necessity?," *NeuroImage*, vol. 53, no. 1, pp. 78–84, 2010.
- [14] M. Brett, A. P. Leff, C. Rorden, and J. Ashburner, "Spatial normalization of brain images with focal lesions using cost function masking," *NeuroImage*, vol. 14, no. 2, pp. 486–500, 2001.
- [15] J. Kim, B. Avants, S. Patel, and J. Whyte, "Spatial normalization of injured brains for neuroimaging research: An illustrative introduction of available options 2008 [Online]. Available: <http://www.nccrn.org>
- [16] J. Sepulcre, J. Goñi, J. C. Masdeu, B. Bejarano, N. Vélaz de Mendizábal, J. B. Toledo, and P. Villoslada, "Contribution of white matter lesions to gray matter atrophy in multiple sclerosis: Evidence from voxel-based analysis of T1 lesions in the visual pathway," *Arch. Neurol.*, vol. 66, no. 2, pp. 173–179, 2009.
- [17] E. I. Zacharaki, C. S. Hogeand, D. Shen, G. Biros, and C. Davatzikos, "Non-diffeomorphic registration of brain tumor images by simulating tissue loss and tumor growth," *Neuroimage*, vol. 46, no. 3, pp. 762–774, 2009.
- [18] N. Hata, T. Dohi, S. Warfield, W. M. Wells, R. Kikinis, and F. A. Jolesz, "Multimodality deformable registration of pre- and intraoperative images for mri-guided brain surgery," in *in Med. Image Computing Computer-Assisted Intervent. (MICCAI)*, Oct. 1998, pp. 1067–1074.
- [19] O. Clatz, H. Delingette, I. F. Talos, A. J. Golby, R. Kikinis, F. A. Jolesz, N. Ayache, and S. K. Warfield, "Robust nonrigid registration to capture brain shift from intraoperative MRI," *IEEE Trans. Med. Imag.*, vol. 24, no. 11, pp. 1417–1427, Nov. 2005.
- [20] K. Rohr, H. S. Stiehl, R. Sprengel, T. M. Buzug, J. Weese, and M. H. Kuhn, "Landmark-based elastic registration using approximating thin-plate splines," *IEEE Trans. Med. Imag.*, vol. 20, no. 6, pp. 526–534, Jun. 2001.
- [21] T. Hartkens, D. Hill, A. Castellano-Smith, D. Hawkes, C. Maurer, A. Martin, W. Hall, H. Liu, and C. Truweit, "Using points and surfaces to improve voxel-based non-rigid registration," in *Proc. Medical Image Computing Computer-Assisted Intervent. (MICCAI)*, 2002, vol. 2489, pp. 565–572.
- [22] S. Periaswamy and H. Farid, "Medical image registration with partial data," *Med. Image Anal.*, vol. 10, no. 3, pp. 452–464, 2005.
- [23] N. Chitphakdithai and J. S. Duncan, "Pairwise registration of images with missing correspondences due to resection," in *Proc. 2010 IEEE Int. Conf. Biomed. Imag. (ISBI)*, 2010, pp. 1025–1028.
- [24] A. Cuzol, P. Hellier, and E. Mémin, "A novel parametric method for non-rigid image registration," in *Proc. Inf. Process. Med. Imag.*, Jan. 2005, vol. 19, pp. 456–467.
- [25] P. Risholm, E. Samset, and I. W. M. Wells, "Validation of a non-rigid registration framework that accommodates tissue resection," in *Proc. SPIE Med. Imag.*, 2010.
- [26] K. O. Babalola, T. F. Cootes, C. J. Twining, V. Petrovic, and C. Taylor, "3-D brain segmentation using active appearance models and local regressors," in *Proc. 11th Int. Conf. Med. Image Computing Computer-Assisted Intervent.—Part I, (MICCAI 08)*, 2008, pp. 401–408.
- [27] A. Trounev and L. Younes, "Metamorphoses through lie group action," *Foundat. Computat. Math.*, vol. 5, no. 2, pp. 173–198, 2005.
- [28] L. Garcin and L. Younes, "Geodesic image matching: A wavelet based energy minimization scheme," in *Proc. EMMCVPR*, 2005, pp. 349–364.
- [29] P. T. Fletcher, S. Venkatasubramanian, and S. Joshi, "The geometric median on riemannian manifolds with application to robust atlas estimation," *NeuroImage*, vol. 45, no. 1, pp. 143–152, 2009, Suppl..
- [30] C. L. Wyatt and P. J. Laurienti, "Nonrigid registration of images with different topologies using embedded maps," in *Proc. IEEE Eng. Med. Biol. Conf.*, 2006, pp. 4823–4827.
- [31] C. L. Wyatt, X. Li, and X. Gong, "A framework for registration of images with varying topology using embedded maps: Riemannian embedding spaces Bioimag. Syst. Lab., Dept. Elect. Comput. Eng. Virginia Polytechnic Inst. State Univ., BSL Report BSL2009-0001, 2009.
- [32] T. Vercauteren, X. Pennec, A. Perchant, and N. Ayache, "Non-parametric diffeomorphic image registration with the demons algorithm," in *Proc. MICCAI*, October 2007, vol. 10, pp. 319–326.
- [33] D. Zosso, X. Bresson, and J. P. Thiran, "Geodesic active fields—A geometric framework for image registration," *IEEE Trans. Image Process.*, vol. 20, no. 5, pp. 1300–1312, May 2011.
- [34] R. Kimmel, N. Sochen, and R. Malladi, "From high energy physics to low level vision," in *Proc. Scale-Space Theory Comput. Vis.*, 1997, pp. 236–247.
- [35] A. Yezzi, S. Kichenassamy, A. Kumar, P. Olver, and A. Tannenbaum, "A geometric snake model for segmentation of medical imagery," *IEEE Trans. Med. Imag.*, vol. 16, no. 2, pp. 199–209, Apr. 1997.
- [36] V. Caselles, R. Kimmel, and G. Sapiro, "Geodesic active contours," *Int. J. Comput. Vis.*, vol. 22, no. 1, pp. 61–79, 1997.
- [37] M. F. Beg, M. I. Miller, A. Trounev, and L. Younes, "Computing large deformation metric mappings via geodesic flows of diffeomorphisms," *Int. J. Comput. Vis.*, vol. 61, no. 2, pp. 139–157, 2005.
- [38] C. Studholme, C. Drapaca, B. Iordanova, and V. Cardenas, "Deformation-based mapping of volume change from serial brain MRI in the presence of local tissue contrast change," *IEEE Trans. Med. Imag.*, vol. 25, no. 5, pp. 626–639, May 2006.
- [39] X. Long and C. L. Wyatt, "Structural template formation with discovery of subclasses," in *Proc. SPIE Med. Imag.*, 2010.
- [40] D. Marcus, T. Wang, J. Parker, J. Csernansky, J. Morris, and R. Buckner, "Open access series of imaging studies (OASIS): Cross-sectional MRI data in young, middle aged, nondemented, and demented older adults," *J. Cognitive Neurosci.*, vol. 19, no. 9, pp. 1498–1507, 2007.
- [41] A. Dale, B. Fischl, and M. Sereno, "Cortical surface-based analysis i: Segmentation and surface reconstruction," *NeuroImage*, vol. 9, no. 2, pp. 179–194, 1999.
- [42] S. Smith, P. R. Bannister, C. Beckmann, J. M. Brady, S. Clare, D. Flitney, P. Hansen, M. Jenkinson, D. Leiboivici, B. Ripley, M. Woolrich, and Y. Zhang, "FSL: New tools for functional and structural brain image analysis," *NeuroImage*, vol. 13, no. 6, 2001.
- [43] Slicer3 [Online]. Available: <http://www.slicer.org/>
- [44] M. Chen, Q. C. W. Lu, K. J. Ruchala, and G. H. Olivera, "A simple fixed-point approach to invert a deformation field," *Med. Phys.*, vol. 35, no. 1, pp. 81–88, 2008.
- [45] M. Luethi, "Inverting deformation fields using a fixed point iteration scheme," *Insight J.*, Jul.–Dec. 2010.